Experimental and numerical investigation of mixing in a partially premixed CH4/H2 combustor

Link, Sarah; Ferrante, Gioele; Dave, Kaushal; Monti, Giulia; Eitelberg, Georg; Domenico, Francesca de

DOI
10.1016/j.ijhydene.2025.05.070

Publication date
2025

Document Version
Final published version

Published in
International Journal of Hydrogen Energy

International Journal of Hydrogen Energy 141 (2025) 176–192

Contents lists available at ScienceDirect

International Journal of Hydrogen Energy

journal homepage: www.elsevier.com/locate/he

Experimental and numerical investigation of mixing in a partially premixed CH_4/H_2 combustor

Sarah Link *,1, Gioele Ferrante *,1, Kaushal Dave, Giulia Monti, Georg Eitelberg, Francesca de Domenico

Flight Performance and Propulsion group, Delft University of Technology, Kluyverweg 1, 2629HS, Delft, The Netherlands

ARTICLE INFO

Keywords:
Jet in swirling cross-flow
Mixing
CH_4/H_2 combustion
Large-Eddy-Simulation
Experimental mixing visualization

ABSTRACT

The mixing of fuel and air is a key factor in determining NO_x emissions during combustion. Lean-premixed burning strategies allow to control the flame temperature and therefore NO_x emissions. However, for highly reactive fuels like hydrogen, the high flame speed makes full premixing dangerous due to the increased risk of flashback. In these cases, current combustor geometries are often operated in partially premixed modes with the fuel injected as close as possible to the combustion chamber. This highlights the need for effective mixing strategies to achieve a high degree of mixing over a short distance. This is even more critical in fuel-flexible combustion systems (e.g., combustors capable of burning both CH_4 and H_2), as the mixing process is heavily influenced by the varying properties of the fuel mixture. In such cases, a comprehensive understanding of the mixing process is required to minimize NO_x emissions under all fuel blends conditions. This paper investigates the mixing of fuel jets into a swirling air cross-flow of a partially-premixed, swirl stabilized combustor using a combined experimental and numerical approach. The injector features an axial swirler and a mixing tube where the air and the fuel jets mix before entering the combustion chamber. The experiments are performed in cold flow conditions. A variable mixture of helium–air is used to represent different blends of CH_4-H_2 fuel, and the mixing process is visualized by seeding the fuel stream with DEHS droplets. Large-Eddy Simulations (LES) confirm the suitability of helium as a surrogate for H_2 by demonstrating similar macro-mixing behavior for the two gases. This study examines the impact of varying fuel composition and momentum flux ratio (J_{swirl}) between the fuel jet and the swirling cross-flow on mixing performance. The results indicate that fuel with lower density achieve better mixing with the air at the mixing tube outlet. A numerical analysis of the radial transport terms reveals that higher H_2 content in the fuel makes it less subject to outward convection which causes stratification close to the mixing tube outlet. Furthermore, the contribution of the molecular diffusion term increases with higher levels of H_2, resulting in improved mixing. When increasing J_{swirl} (up to J_{swirl} = 10) increases the penetration of the fuel jet into the swirling flow. Above a critical value of J_{swirl}, the mixture homogeneity at the mixing tube outlet becomes insensitive to J_{swirl} for the investigated geometry. Overall, the fuel composition was found to have a greater influence on the level of mixing close to the mixing tube outlet than variations in J_{swirl}.

1. Introduction

Hydrogen is a highly promising alternative fuel for decarbonization in many industrial applications, largely due to its carbon-free combustion [1,2] and the possibility of producing it through renewable energy via water electrolysis. However, challenges related to the production, transport and storage of (green) H_2 [3,4] currently limit its large-scale adoption, creating uncertainty regarding its availability in the near future. Fuel-flexible combustion systems capable of operating on both carbon-based fuels and H_2 or any mixture of the two (up to 100% H_2), have attracted significant interest across various industries in recent years. However, the significantly different combustion characteristics of H_2 compared to carbon-based fuels present challenges when used in the same combustion chamber design. In combustors burning hydrocarbon fuels, fully premixing fuel with oxidizer and operating in lean conditions, is a common strategy to reduce NO_x emissions by ensuring a uniform temperature distribution [5]. For H_2, which has a significantly higher flame speed than carbon-based fuels, the risk of flashback and

* Corresponding authors.
E-mail addresses: s.j.link@tudelft.nl (S. Link), g.ferrante@tudelft.nl (G. Ferrante).
[1] Sarah Link and Gioele Ferrante have contributed equally to this work.

https://doi.org/10.1016/j.ijhydene.2025.05.070
Received 10 March 2025; Received in revised form 28 April 2025; Accepted 6 May 2025
Available online 2 June 2025

thermoacoustic instabilities is considerably increased [6]. To mitigate these risks and stabilize flames with high H_2 content, a partially premixed injection strategy is often employed [7–9]. The fuel is injected as late as possible upstream of the combustion chamber, while still ensuring adequate mixing with the oxidizer. Efficient mixing offers several advantages, including a reduction of NO_x emissions [5,10,11], but also a reduction in the number of fuel injection nozzles required for operation, simplifying the manufacturing process [12]. A widely used approach to achieve efficient mixing is the jet in cross-flow configuration (JICF), in which the fuel is injected transversely into the oxidizer flow [13,14]. This method is commonly employed in technical applications requiring efficient fuel–air mixing, such as fuel injection into burners for gas turbines or even scramjets [15].

The flow development in a JICF configuration with an axial cross-flow involves four key structures: (1) horseshoe vortices originating from the jet, (2) windward rolling vortices from Kelvin–Helmholtz instability, (3) a counter-rotating vortex pair (CVP) dominant in the far field, and (4) upright vortices in the jet's wake from cross-flow boundary layer vorticity. The CVP is critical for mixing the jet with the surrounding fluid, by entraining cross-flow fluid into the jet [16,17]. The mixing performance is affected by the geometry of the nozzle [18, 19] and the injection angle [20], as they influence the strength and type of vortical structures. For a given geometry, the mixing is primarily determined by the jet to cross-flow density ratio $S = \rho_{\mathrm{jet}}/\rho_{\mathrm{crossflow}}$, the jet to cross-flow velocity ratio $R = U_{\mathrm{jet}}/U_{\mathrm{crossflow}}$, the jet to cross-flow momentum flux ratio $J = SR^2$ and the flow Reynolds numbers Re [13,21,22]. It has been widely concluded that the momentum flux ratio J is the most significant parameter governing the degree of mixing [23,24]. The results show that, to achieve effective mixing, J tends to exceed 25, in some cases it even exceeds $J > 100$ [23]. At very high values of J ($J > 100$), the jet behaves more like a free jet in a static flow [25]. Conversely, for low values of J ($J < 1$), the jet adheres to the wall rather than penetrating into the cross-flow, a behavior commonly used for film cooling in turbine blades [26]. Moreover, the high diffusivity of jet fluids like H_2 is expected to have a substantial impact on the mixing process [27].

More complex cross-flows involve swirling flows, which are often used to stabilize flames in modern gas turbines [28,29]. If the swirl number is high enough, a central recirculation zone is formed, which aerodynamically stabilizes the flame in the combustion chamber away from the solid components [30]. The mixing of transverse jets with a swirling cross-flow introduces further complexities, as the flow additionally has a tangential velocity component and a radial pressure gradient. Early research into this interaction focused on the mixing of helium jets discharged transversely into a swirling flow [31,32], to account for a density difference between the jet and the cross-flow. The swirl was found to have a strong effect on the penetration depth of the jet into the cross flow, reducing it by a factor of 5 for a swirl number of $Sw = 2.25$ [31]. On the other hand, the reduced jet penetration depth is counteracted by the low density of helium ($\rho_{\mathrm{He}}/\rho_{\mathrm{air}}$). In facts, the air stream is more subject to centrifugal forces than helium due to its higher density, which promotes the transport of helium towards the center of the swirling flow [32]. For momentum flux ratios 0.28 $\leq J \leq$ 12.6 the jets follow a spiral path and advance in the same direction as the swirling flow. More recently, Tan et al. [33] explored the mixing mechanisms of H_2 transverse jets in swirling cross-flows. Their findings suggest that increasing the swirl number affects mixing by forming a central recirculation zone and altering the distribution of shear layers within the flow. The momentum flux ratio affects the mixing by influencing the velocity of the jet and the uniformity of the flow.

Swirling flows and jet-in cross-flow configurations with axial cross-flow have been studied individually extensively in literature. However, there remains a limited understanding of how different parameters interact to determine mixing efficiency in jet in cross-flow setups with swirling cross-flow. In particular, no studies have accounted for the effects of varying fuel densities on the mixing process, nor has a systematic methodology been established to investigate these effects experimentally and numerically. Understanding the effects of fuel injection parameters and composition on the overall mixing behavior is crucial for assessing NO_x trends and flashback propensity in partially premixed fuel-flexible swirl-stabilized burners by identifying regions of fuel accumulation. The present study aims to fill the gap in literature by investigating the mixing characteristics of a jet in swirling cross-flow configuration in the dual-fuel (CH_4/H_2) partially premixed combustor developed at TU Delft [34,35], through a combined numerical and experimental approach. Helium/air mixtures are used as a substitute for the CH_4/H_2 fuel mixture while maintaining a constant mixture density. Experimentally, seeding the jet stream with droplets allows to visualize the mixing process and velocity fields in an optically accessible mixing tube. Large-Eddy Simulations validate this approach by examining the mixing properties of both the original fuel and its helium/air surrogate. By varying the momentum flux ratio J and fuel composition, this research aims to clarify the key factors for achieving optimal mixing in fuel-flexible combustion systems that operate with substantially different fuels. Additionally, the numerical simulations provide insights into the contribution of different transport terms (convection, molecular diffusion and turbulent diffusion) to the mixing process.

This paper is organized as follows. Section 2 explains the design of the combined numerical and experimental study, along with a description of both set-ups. Section 3 validates the LES simulation with experimental data, and evaluates the use of helium as a tracer for H_2. Additionally, the mixing behavior under varying fuel composition and momentum flux ratios (J) is examined. Section 4 summarizes the key findings of this study, while Section 5 outlines future work and discusses related considerations.

2. Methodology

2.1. Burner geometry

The present study investigates the fuel/air mixing process within the TU Delft partially premixed swirl-stabilized combustor, featuring a jet in swirling cross-flow fuel injection configuration. A schematic of the set-up is provided in Fig. 1. The air is supplied through an axial swirler with an analytical swirl number of $Sw_{\mathrm{geom}} = 1.1$ [36]. This study focuses on the operating conditions outlined in [34], where the burner operates under different CH_4/H_2 mixtures with a constant thermal power $P = 12\,\mathrm{kW}$ and a constant mass flow rate of air, consequently only the fuel flow rates change (see Table 1, left side). When fuel mixtures with a high percentage of H_2 are burnt, the axial air injection (AAI) strategy is adopted to prevent flashback. This is achieved by injecting part of the combustion air non-swirling on the centerline of the mixing tube through a channel, visible in the center of the swirler in Fig. 1. However, this study only focuses on conditions without AAI. Downstream of the swirler exit, the fuel gets injected perpendicular to the swirling flow through 4 injection ports. The size of the fuel ports in the reacting case is $d_{\mathrm{fuel}} = 3.5\,\mathrm{mm}$.

The mixing of fuel and air takes place in the mixing tube with a diameter of $d_{\mathrm{MT}} = 24\,\mathrm{mm}$ and length $l_{\mathrm{MT}} = 60\,\mathrm{mm}$. Downstream of the mixing tube, the mixtures enters the combustion chamber, with a diameter of $d_{\mathrm{CC}} = 148\,\mathrm{mm}$ and $l_{\mathrm{CC}} = 400\,\mathrm{mm}$. The reference frame is set with its origin on the mixing tube axis, at the combustion chamber entrance, with the y-axis aligned with the flow streamwise direction.

2.2. Combination of experimental and numerical design

The mixing process of fuel and air in a jet in swirling cross-flow configuration is complex and influenced by many parameters, especially in set-ups operating with various mixtures of CH_4 and H_2. When studying the mixing of fuel and air, using a non-reactive surrogate gas is beneficial, as it eliminates the complexities associated with handling reactive

Table 1
Volumetric flow rates of fuel mixtures and diameters of the fuel injection ports for the reacting experiments (CH_4/H_2) [34] and the corresponding surrogate fuel mixtures (He/air) at p = 1 atm and T = 288.15 K.

CH_4/H_2 reacting case at $P = 12$ kW					He/air surrogate					
Tag	XH_2	Q_{H2} [lpm]	Q_{CH4} [lpm]	d_{fuel} [mm]	Tag	Q_{He} [lpm]	Q_{air} [lpm]	$d_{J,low}$ [mm]	$d_{J,mid}$ [mm]	$d_{J,high}$ [mm]
A	0	0	21.21	3.5[a]	A_s	11.01	10.58	3.5[b]	1.6	1.4
B	0.4	11.17	16.76	3.5[a]	B_s	22.27	7.82	3.5[b]	1.6[b]	1.4[b]
C	0.8	39.2	9.13	3.5[a]	C_s	42.87	2.25	3.5[b]	1.6	1.4
D	1	71.8	0	3.5[a]	D_s	71.80	0	4.1[a,b]	1.9[b]	1.6[b]

[a] The set points simulated with LES are indicated.
[b] Denotes the conditions analyzed only experimentally.

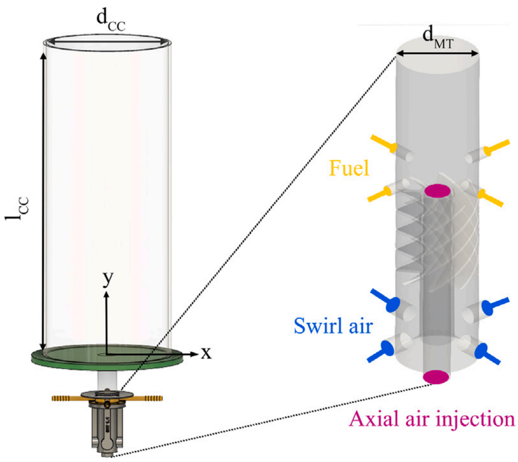

Fig. 1. Schematic of the experimental setup with the reference coordinate system, including a detailed view of the injector with jet-in-swirling cross-flow fuel inlets and the axial air injection port.

gases. Helium (He) has previously been proposed as a surrogate for H_2. Although it does not replicate the micro-mixing characteristics of H_2 with oxidizers, previous results suggest that it exhibits a similar global mixing behavior [37]. Following the flow parameters outlined in [21], it is desirable to match the jet velocity, density, and Reynolds number in non-reactive scenarios with those of reacting cases.

In this work, He/air mixtures are used as a surrogate for CH_4/H_2 mixtures, matching both the density and injection velocity of the jet, while maintaining the same fuel inlet diameter.

To represent the 100% H_2 case using helium as a surrogate, it is not possible to match the fuel density, since He is approximately twice as dense as H_2. Therefore, to maintain the same momentum flux ratio J, the volumetric flow rate of the fuel stream is kept constant between H_2 and He, and the fuel inlet diameter is increased when using He. Table 1 shows the fuel compositions for the reacting case (Tag A - D) and the corresponding fuel surrogates (Tag A_s - D_s) for the non-reacting experiment.

Beyond examining the effect of fuel composition on mixing, this study also investigates the influence of the momentum flux ratio J_{swirl} on the mixing. The momentum flux ratio between transverse jets and swirling cross-flows is defined as follows [33]

$$J_{swirl} = \frac{\rho_{jet} \cdot U_{jet}^2}{\rho_{air} \cdot U_{air}^2 \cdot (1 + 4 \cdot Sw^2)} \tag{1}$$

where ρ is the density and U the axial velocity. In this paper, U_{air} is taken as the bulk velocity of the swirling air, due to the complex velocity distribution at the swirler outlet. In addition to the baseline case (J_{low}) representing the surrogate conditions of the reacting case, two higher momentum flux ratios were investigated (J_{mid} and J_{high}), calculated according to Eq. (1). This was achieved by decreasing the diameter of the fuel injection ports and keeping the flow rates constant. The diameters for the different momentum flux ratios at the different fuel compositions are summarized in Table 1.

Fig. 2(a) shows the momentum flux ratio J_{swirl} by varying the percentage of H_2 in the fuel for the reacting cases (CH_4/H_2, blue line) and its surrogate (He/air, J_{low}, green dotted line). The blue line contains more data points because more conditions were tested in the reacting conditions than in the surrogate conditions. It can be seen that the curves of the two mixtures match well, since the density is kept constant between the fuel mixture and the surrogate fuel. For both, the momentum flux ratio increases up to $XH_2 = 0.8$, and afterwards drops again slightly. Fig. 2(b) shows the momentum flux ratios for all the diameters investigated (J_{low}, green dotted line, J_{mid}, red dotted line, and J_{high}, cyan dotted line). Instead of maintaining a constant J_{swirl} across the different cases, the fuel inlet diameter was kept constant to better represent a realistic scenario. However, once again for the surrogate case of $XH_2 = 1$, the diameter was increased, to avoid a significant increase of J_{swirl} with respect to the other fuel compositions. Fig. 2(c) shows the corresponding Reynolds numbers for the cases displayed in Fig. 2(b). Due to the higher viscosity of Helium compared to H_2 and CH_4, some discrepancies are observed in the Reynolds numbers between the reacting fuel and its surrogate at the same value of J_{swirl} (blue and green data). Additionally, as expected, decreasing the fuel injection diameter results in an increase in the Reynolds number. However, for all investigated cases, the flow remains in the laminar or transition regime. Therefore, the change in Reynolds number is not anticipated to affect the mixing substantially.

The investigation of the mixing process is carried out within a combined numerical and experimental framework, which is schematically visualized through the flow chart in Fig. 3. The influence of surrogate fuel composition on the mixing is assessed experimentally, as well as the effect of the momentum flux ratio (J_{swirl}) on the mixing process. This approach is chosen due to the broad parameters space and the flexibility of the experimental setup, which allows for easy adjustment of the fuel inlet diameters to achieve the desired momentum flux ratios.

In addition to the experiments, some test cases are investigated numerically through Large Eddy Simulations (LES) with a multi-component mixture model to simulate the turbulent mixing process. The numerical results provide quantitative details about the fuel mass fraction distribution in the mixing tube and combustion chamber. The 100% helium case (D_s in Table 1) is simulated to validate the numerical model through the comparison of results with experimental measurements. Then, the cases involving different CH_4/H_2 fuel compositions (cases A, C and D in Table 1) are analyzed. A comparison between case D and D_s allows to assess the suitability of helium as a surrogate tracer to represent the macroscopic mixing features of H_2. The mixing quality is analyzed for the different fuel mixtures and the trends are compared to experimental results for the surrogate cases. The analysis of the terms in the mass fractions transport equations allows to assess the relative relevance of convection, molecular diffusion and turbulent transport in the mixing process of the various species.

2.3. Experimental set-up and methodology

Experiments were performed in a 3D-printed duplicate of the TU Delft partially premixed CH_4/H_2 swirl-stabilized burner [34,35]. The

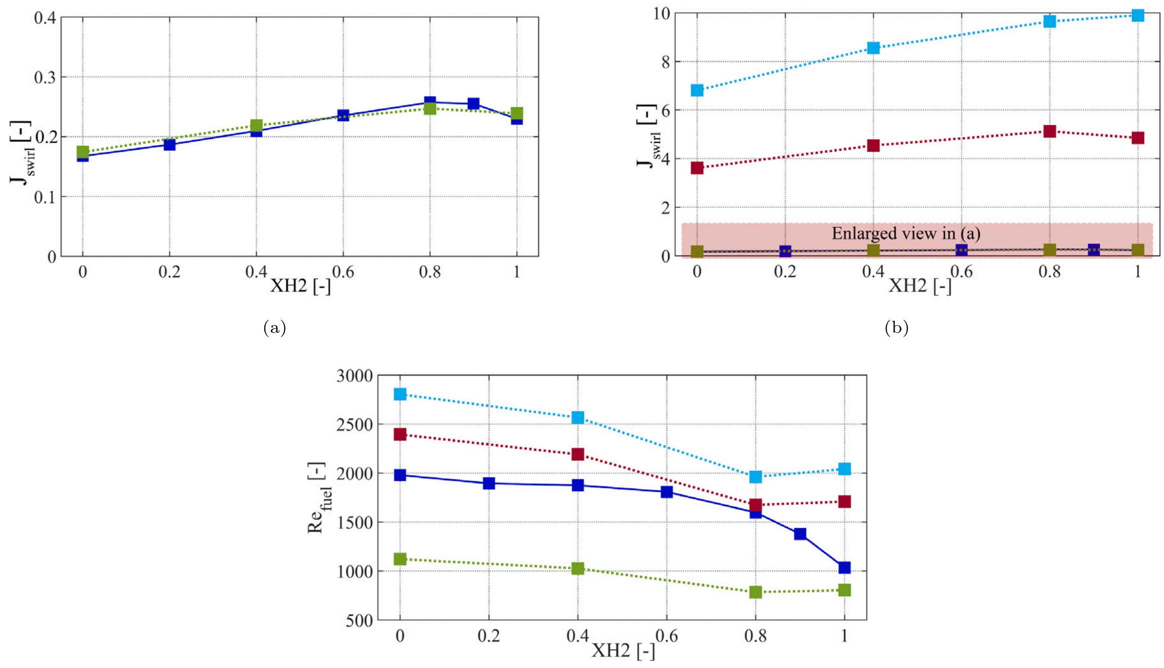

Fig. 2. (a) Momentum flux ratio for CH_4/H_2 mixtures (▬) and the surrogate conditions (····), (b) Momentum flux ratios and Re numbers (c) in the fuel nozzles for CH_4/H_2 mixtures (▬) and the surrogate fuel at different momentum flux ratios J_{swirl}: low(····), mid (····) and high (····). (a) is a zoomed version of (b). (For interpretation of the references to color in this figure legend, the reader is referred to the web version of this article.)

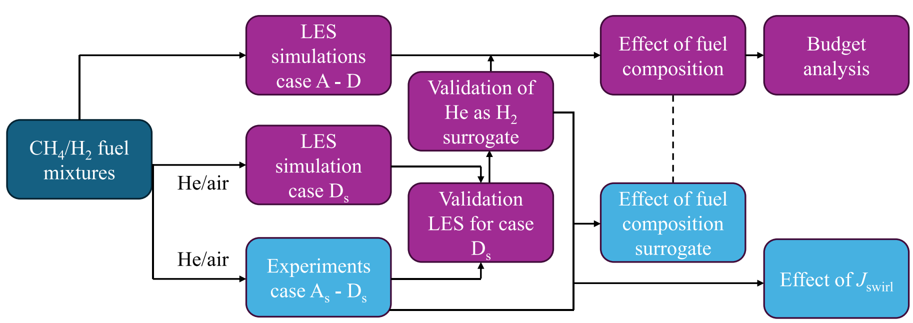

Fig. 3. Flowchart of the experimental and numerical framework, with purple boxes representing numerically investigated steps and blue boxes representing experimentally investigated steps. (For interpretation of the references to color in this figure legend, the reader is referred to the web version of this article.)

stainless steel axial swirler is reused from the reacting swirl-stabilized set-up to maintain consistency in the injector geometry. The combustion chamber and mixing tube are made from acrylic, to allow optical access. The wall thickness of the combustion chamber is 3 mm, and that of the mixing tube is 0.9 mm. The small wall thickness for the mixing tube was chosen to reduce reflections and distortion close to the walls. During the experiments, the mass flow rates for both air and helium were controlled by Bronkhorst digital mass flow meters with an accuracy of ±0.5% RD plus ±0.1% FS.

The mixing process was analyzed using Mie scattering images acquired inside the mixing tube. Since only the fuel stream was seeded, the Mie scattering signal provides a good approximation of the mixing level between the fuel and air streams. For this purpose, the surrogate fuel stream (He/air) was seeded with DEHS droplets with a droplet size of 0.9 μm (peak of q3 size distribution), generated using a PIVTEC PIVpart45 seeder. The Stokes number for the droplets is $St < 0.1$ for all J_{low} and J_{mid} cases based on the fuel inlet diameter and the fuel bulk velocity. For the J_{high} cases, due to the high velocities the Stokes number is $St < 0.18$. The Stokes number indicates that the particle response time is sufficiently low to track large-scale flow structures,

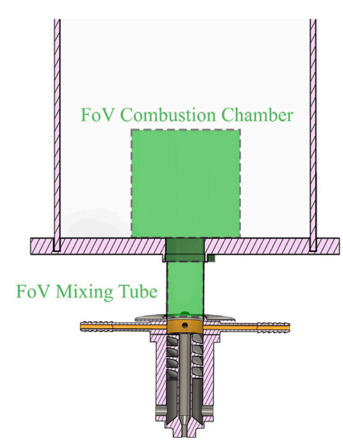

Fig. 4. Field of view for the optically accessible combustion chamber and mixing tube.

providing a reliable measure of the average macroscopic mixing [38]. However, since the local Stokes numbers might be locally higher in shear layers, small-scale turbulent mixing may not be accurately resolved. Additionally, the significantly higher density of DEHS droplets compared to helium, combined with centrifugal forces in swirling flows, may cause the DEHS droplets to move outward from the vortex core. Moreover, DEHS droplets do not replicate the molecular diffusion behavior of helium.

The particles for visualizing the mixing process were illuminated by a 527 nm high-repetition-rate (1 kHz) laser with a pulse energy of 30 mJ and a pulse width of <200 ns (Quantronix Darwin Duo 527-80-M). The scattered light was captured with a Photron Fastcam Mini AX 100 (sensor size 1024 × 1024 pixels) with a repetition rate of 1 kHz. The camera was mounted with a macro lens (105 mm, fstop 8). The laser and the camera were synchronized with a PTU X in the software Davis 10. The field of view for the particle imaging in the combustion chamber and the mixing tube can be seen in Fig. 4. Due to the baseplate of the combustion chamber, the range between $-11\,\mathrm{mm} < y < 0\,\mathrm{mm}$ is not optically accessible.

In addition to the mixing fields, the flow fields in the mixing tube and the combustion chamber were obtained using 2D2C Particle Image Velocimetry (PIV) with the same laser and camera set-up and the same acquisition parameters. The two laser pulses had a Δt of $10\,\mu\mathrm{s}$ for measurements in the combustion chamber, and Δt of $20\,\mu\mathrm{s}$ for measurements in the mixing tube. The velocity fields were computed with the cross-correlation algorithm (LaVision, Davis 10 software). A multipass cross-correlation approach with decreasing interrogation window size (from 128 × 128 to 16 × 16 pixels) is applied to obtain the instantaneous velocity vectors in the combustion chamber. The final interrogation window size with 75% overlap yields a vector spacing of approximately 0.11 mm. For the mixing tube, a multipass cross-correlation approach with a decreasing interrogation window size (from 64 × 64 pixels to 12 × 12 pixels) is applied, which results in a vector spacing of around 0.12 mm. The data was filtered for outliers (Davis 10 universal outlier detection with median filter) and interpolated from adjacent interrogation areas. The velocity fields are averaged over 2000 images. The post-processing of Mie-scattered images and the evaluation of mixing quality are discussed later in Section 2.5, as the same method for evaluating the degree of mixing is used for both experiments and LES simulations.

2.4. Numerical set-up and methodology

2.4.1. Large eddy simulations

Large eddy simulation (LES) paradigm is employed for the numerical analysis of the present case. LES approach allows to directly resolve most of the turbulent flow field and mixing phenomena, while the effect of small turbulent structures falling below the computational grid resolution (subgrid scales sgs) is modeled. The considered fluid is a multicomponent mixture whose composition, and therefore density, vary through the mixing process. To deal with non-constant density, a Favre-filtered (density-weighted) formulation of the Navier–Stokes equations is employed. The Favre-filtering operator for a generic quantity is defined as $\widetilde{\psi} = \frac{\overline{\rho\psi}}{\overline{\rho}}$, where the overline represents the LES filter and ρ is the mixture density [39]. The filtered continuity and momentum conservation equations are expressed as:

$$\frac{\partial\overline{\rho}}{\partial t} + \frac{\partial(\overline{\rho}\tilde{u}_i)}{\partial x_i} = 0 \tag{2}$$

$$\frac{\partial(\overline{\rho}\tilde{u}_i)}{\partial t} + \frac{\partial(\overline{\rho}\tilde{u}_i\tilde{u}_j)}{\partial x_j} = -\frac{\partial\overline{p}}{\partial x_i} + \frac{\partial\overline{\tau}_{ij}}{\partial x_j} + \frac{\partial\tau_{ij}^{\mathrm{sgs}}}{\partial x_j} \tag{3}$$

where p and u_i represent the pressure and velocity components, respectively and $\overline{\tau}_{ij}$ denotes the resolved viscous stress tensor. The subgrid viscous stress tensor is modeled using the eddy diffusivity approach, such that $\overline{\tau}_{ij} + \tau_{ij}^{\mathrm{sgs}} = -2(\widetilde{\mu} + \mu_{sgs})\left(\widetilde{S}_{ij} - \widetilde{S}_{kk}\delta_{ij}/3\right)$, where $\widetilde{S}ij$ is the Favre-filtered strain tensor, and δij is the Kronecker delta. The dynamic viscosity for each species μ_k is calculated as a polynomial function of the logarithm of temperature, T, using the species transport properties according to the San Diego chemical mechanism in [40]. From the μ_k values, a simple mass fraction based average is applied to determine the dynamic viscosity of the whole mixture, μ. The subgrid-scale viscosity, μ_{sgs}, is derived from the kinematic sgs viscosity, modeled through a one-equation approach [41]: $\nu_{sgs} = c_k k_{sgs}^{1/2}\Delta$, where Δ is the LES filter width, $C_k \approx 0.094$ is a model constant and k_{sgs} is the subgrid-scale turbulent kinetic energy, obtained by solving an additional transport equation. This turbulence model is particularly well-suited for flows with anisotropic turbulence, such as the present case involving swirling motion and transverse injection. The solution of a transport equation allows to capture the dynamic behavior of the subgrid turbulence field with its spatial inhomogeneities and temporal variations.

To analyze the mixing process, an additional transport equation is resolved for the mass fractions Y_k of each species composing the mixture (i.e. N_2, O_2, H_2, He, CH_4). Setting to zero the source term associated to chemical reactions, the transport equation reduces to a convection–diffusion equation:

$$\frac{\partial(\overline{\rho}\widetilde{Y_k})}{\partial t} + \frac{\partial(\overline{\rho}\tilde{u}_j\tilde{Y}_k)}{\partial x_j} = \frac{\partial}{\partial x_j}\left[\left(\overline{\rho D_k^m} + \frac{\mu_{sgs}}{Sc_t}\right)\frac{\partial\widetilde{Y_k}}{\partial x_j}\right] \tag{4}$$

The effective diffusion coefficient on the right-hand side term consists of two contributes: one representing species transport due to molecular diffusion and another accounting for subgrid convective transport. The latter is modeled as an additional diffusion term with a diffusion coefficient $D_t = \mu_{sgs}/Sc_t$. A constant turbulent Schmidt number is used for all the species, set to $Sc_t = 0.7$. A mixture-averaged model following Fick's law approximation [42] is employed to determine the molecular diffusion coefficient of each species k with respect to the mixture:

$$D_k^m = \frac{(1 - Y_k)}{\Sigma_{j\neq k}^N X_k/D_{kj}} \tag{5}$$

where X_k are the species mole fractions, and D_{kj} are the binary diffusion coefficients for each species pair, expressed as a logarithmic polynomial function of temperature, following [40]. This approach ensures that the diffusion coefficient of each species varies in time and space according to the local mixture composition. Unlike the equi-diffusivity assumption, it captures inter-species diffusion more accurately and accounts for its effects on resolved scales mixing, including, for example, separation phenomena in multicomponent fuels.

An energy conservation equation is also solved, as no incompressibility assumption is made. A filtered transport equation for the sensible enthalpy h_s is therefore solved:

$$\frac{\partial(\overline{\rho}\widetilde{h}_s)}{\partial t} + \frac{\partial(\overline{\rho}\widetilde{u}_j\widetilde{h}_s)}{\partial x_j} = \frac{\partial\overline{p}}{\partial t} + \frac{\partial}{\partial x_j}\left[\left(\overline{\rho\alpha} + \frac{\mu_{sgs}}{\mathrm{Pr}_t}\right)\frac{\partial\widetilde{h}_s}{\partial x_j}\right] + \frac{\partial}{\partial x_j}\left(\sum_{k=1}^{N}\overline{\rho D_k^m}\widetilde{h_k^s}\frac{\partial\widetilde{Y_k}}{\partial x_j}\right) \tag{6}$$

where α denotes the thermal diffusivity, computed analogously to the dynamic viscosity and the turbulent Prandtl number is taken equal to $Pr_t = 0.85$. The equation set is closed through the filtered ideal gas equation of state and the thermodynamic relation $h_s = \int_{298.15K}^{T} C_p(T')dT'$, where Cp is the mixture's specific heat at constant pressure, computed through Janaf polynomials [40].

2.4.2. Numerical setup

The Favre-filtered Navier–Stokes equations are resolved in OpenFOAM v9 through finite volumes method. The reactingFoam solver is utilized, which supports models for multicomponent mixtures, but chemical reactions are disabled to focus solely on species mixing simulation. Pressure–velocity coupling is solved via the PISO (Pressure-Implicit with Splitting Operator) algorithm with three iterations per step, supplemented by an outer SIMPLE loop (Semi-Implicit Method for

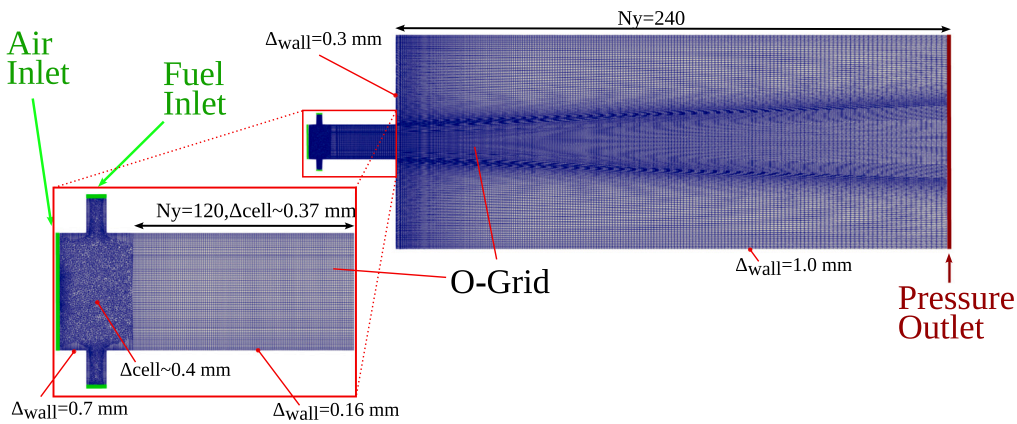

Fig. 5. Sketch of the computational grid.

Pressure Linked Equations) that executes two iterations per time step to handle the other scalar transport equations such as energy, species and turbulent kinetic energy. Convective terms are discretized with a second-order central differencing scheme, with an upwind limiter for regions of strong gradients. The temporal discretization relies on a second-order implicit backward scheme with a constant time step of $\Delta t = 2 \times 10^{-7}$ s, ensuring a CFL number below 0.5 in the mixing tube and combustion chamber entrance regions.

The numerical domain, illustrated in Fig. 5, includes the combustion chamber, the mixing tube, and the fuel ports, according to the geometry detailed in Section 2.3. The swirler is excluded from the calculation to reduce the computational cost and a synthetic turbulence generator [35,43] is employed to mimic the turbulent swirling flow delivered at the swirler exit, as described next. A hybrid structured/unstructured meshing approach is used, to exploit the advantages of hexahedral elements in terms of cell skewness and non-orthogonality minimization, but retaining the flexibility of tetrahedral cells to discretize the regions with more complex geometry. The mixing tube is discretized through an O-grid where the hexahedral cells have a characteristic size of $\Delta_{\mathrm{cell}} = 0.3λ0.4$ mm. A non-uniform spacing is imposed to refine the wall region, where the first cell height is set to $\Delta_{\mathrm{wall}} = 0.16$ mm corresponding to $y^+_{wall} < 10$ under fully developed flow. The O-grid extends to the combustion chamber, maintaining a cell size of $\Delta_{\mathrm{cell}} = 0.3λ0.4$ mm in the mixing tube exit region, and merges with an additional annular structured block. An unstructured block with tetrahedral cells with a characteristic size of $\Delta_{\mathrm{cell}} = 0.5$ mm is used in the region connecting the fuel ports to the mixing tube. A wall refinement is obtained here through hexahedral layers achieving a first cell height of $\Delta_{\mathrm{wall}} = 0.07$ mm. The total cell count is 4.45 M.

The mesh quality was assessed a-posteriori through Pope's criterion [44], verifying that the subgrid turbulent kinetic energy represented less than the 20% of the total turbulent kinetic energy (resolved plus subgrid) $k_{sgs} < 20\%\mathrm{TKE} = 20\%(K + k_{sgs})$ in the region of interest. Additionally, a mesh sensitivity analysis was conducted by performing an LES simulation of case D_s on a finer, fully block-structured grid containing 12.14 million hexahedral elements, which discretized the entire domain, including the swirler. A comparison of the predicted time average velocity and species mass fractions fields (not shown) confirmed that the LES results are mesh insensitive for macroscopic quantities.

The same simulation was used to characterize the turbulent flow field at the swirler exit and provide accurate inlet conditions for the simulations where the swirler is excluded from the computational domain. Time-averaged fields of the three velocity components U_j and the six components of subgrid velocity variances (and covariances) $\overline{u_i u_j}$ were extracted on a surface at an axial location of $x = -60$ mm and imposed as target conditions to a synthetic turbulence generator [43], along with an integral turbulent length scale of about $l_t \sim 1/3 D_h$, where $D_h \sim 6$ mm is the hydraulic diameter of a single swirler vane. The synthetic turbulence generator produces time-varying inlet velocity values at every face of the air inlet patch (see Fig. 5), ensuring that the first and second-order time statistics of the generated velocity field match the prescribed target values. The velocity field statistics obtained from the simplified geometry were compared against those from a refined mesh with the swirler fully resolved. The comparison confirmed that the synthetic turbulence method accurately reproduces the relevant turbulent features in mixing tube and combustion chamber, thereby validating its use. A constant mass flow rate at a temperature of $T = 288.15$ K is applied at the fuel ports, consistently with the considered operating conditions, reported in Table 1. Zero pressure gradient is imposed to every inlet. Zero normal gradient velocity and wave transmissive pressure boundary conditions are imposed at the domain outlet to mitigate the reflection of pressure waves back to the swirler, with atmospheric pressure set at a distance $l = 3$ m from the combustion chamber outlet [45,46] . No-slip conditions are applied to the velocity at the walls and zero-gradient to other quantities. In regions where the wall refinement is insufficient to resolve the boundary layer, Spalding wall functions are employed to approximate the subgrid turbulent viscosity [47]. As mentioned in Section 2.4.1, the thermochemical properties of the considered species are taken accordingly to the San Diego kinetic mechanism [40].

In the present set-up, preliminary LES showed a wide range of residence time values in the different regions of the computational domain, depending on the various flow features, such as the recirculation zones originating in the combustion chamber. For this reason, each simulation is initialized from an LES solution evolved for $t_{\mathrm{chamb}} = 1.5$ s, which is the total amount of time necessary for a fluid parcel to travel from the swirler ports to the outlet of the combustion chamber, in order to obtain a fully developed air flow field. A smaller characteristic time $t_{\mathrm{flow}} = 0.1$ s is chosen, coinciding with the flow residence time at the mixing tube exit, at a location of $y = 25$ mm. Therefore, each LES is run for one characteristic time for further fuel stream development after the initialization, and for additional 2 t_{flow} to acquire statistics, for a total of $t_{\mathrm{tot}} = 0.3s$. On the 4.45 M mesh, without resolving the swirler, a typical simulation requires 30'000 CPU-hours to compute one characteristic time t_{flow}. The LES settings are summarized in Table 2.

2.4.3. LES setup summary

In the considered case density is not constant due to mixing of two different flows therefore the Favre-filtered (density weighted) LES equations are solved. A transport equation for each species is solved, in order to accurately capture the mixing process. A mixture-averaged diffusion model is adopted to accurately compute the local species diffusion coefficients. This allows to capture differences in mixing due to the diffusivity of the fuel mixtures, e.g. considering the higher diffusivity of H_2 and He with respect to air and methane. A one equation k_{sgs}

Table 2
LES simulation settings.

Parameter	Value	Parameter	Value
n_{cells}	4.45 M	Δ_{cell}	0.3–0.4 mm
y^+_{wall}	<10	Wall functions	Spalding [47]
Time step Δt	2×10^{-7} s	$CFL_{\max}$	0.5
Solver	reactingFoam compressible	Temporal integration	Second-order implicit backward
t_{tot}	0.3 s	Subgrid turbulence model	One-equation k_{sgs} [41]
t_{flow}	0.1 s	Computational cost	30k CPU-hours/t_{flow}

subgrid-scale turbulence model is used, which is especially well-suited for representing anisotropic turbulence, such as that found in the jet in swirling crossflow configuration analyzed in this study. To reduce computational cost, the domain does not include the swirler, instead, a synthetic turbulent inflow generator is applied at the mixing tube inlet, resulting in a mesh of approximately 4.45 million cells. The reference turbulent inflow field is derived from a previous LES on a finer mesh (12.14 million cells) that explicitly includes the swirler geometry. This allows to reduce the required computational resources from 50'000 CPU-hours to 30'000 CPU-hours for the simulation of one characteristic flow time $t_{\text{flow}} = 0.1$ s.

2.5. Evaluation of mixing quality

This section discusses how the mixing is evaluated experimentally and numerically. Fig. 6 shows the experimental methodology to determine the particle concentration from Mie scattering images acquired in the mixing tube. The raw images on the left show the single shot data acquired for case A_s, J_{low} (top) and case D_s, J_{high} (bottom). Since the fuel stream is seeded, the particle distribution within the mixing tube reflects the degree of mixing. Greater penetration of seeding particles into the center of the mixing tube indicates a higher degree of mixing. It is evident that the raw image in the top row demonstrates worse mixing compared to the raw image in the bottom row, as the particles do not reach the center of the mixing tube. After subtracting the minimum sliding background (filter length = 9 images), the noise floor was determined by the 10 percentile of the pixel intensities. A Signal to Noise (SNR) ratio of 2.5 was chosen, in order to guarantee a sufficiently high signal. The noise multiplied with the SNR gives the threshold. Pixel with an intensity below the threshold are set to 0, particles above this threshold are set to 1 (second column of Fig. 6, step binarization). Afterwards, the particles per pixel were counted in a time-series of 200 statistically independent images. After calculating the average, the signal is normalized by its maximum value, and a smoothing filter with a filter size of 25 × 25 pixels is applied.

The mixing quality of the configuration is evaluated for both experiments and LES simulation with the spatial unmixedness parameter U_s, which is the ratio of the spatial variance in fuel concentration in a given plane to the maximum spatial variance of the same quantity, and is defined as [48]

$$U_s(y) = \frac{\langle (\overline{C(x,y)} - \langle \overline{C(y)} \rangle)^2 \rangle}{\langle \overline{C(y)} \rangle \cdot (1 - \langle \overline{C(y)} \rangle)} \tag{7}$$

$\overline{C}$ expresses the temporal average, and $\langle C \rangle$ expresses the spatial average of C. Consequently, $\langle (\overline{C(x,y)} - \langle \overline{C(y)} \rangle)^2 \rangle$ refers to the variance of the fuel concentration C and $\langle \overline{C(y)} \rangle$ to the average of the concentration C at a given y-location. For the LES simulation, C refers to the fuel mass fraction Y_{fuel}, in the experiments C refers to the particle concentration. Since no three-dimensional data are available from the experiments, the degree of mixing is evaluated with planar data of the fuel distribution C for both, experimental data and LES. U_s lays between 0 for a perfectly premixed system and 1 for totally unmixed system.

Besides this scalar parameter, a spatial distribution of the normalized fuel concentration is used to show how the fuel distributes throughout the measurement plane

$$C^*(x,y) = \overline{C(x,y)} / \langle \overline{C(y)} \rangle \tag{8}$$

C^* is a useful parameter to compare cases with substantially different fuel compositions, as the fuel mass fraction is locally normalized by its spatial average at each stream-wise location. An example plot of C^* for the experimental data can be seen in Fig. 6 in the right column, which shows the normalized particle distribution C^*, calculated after averaging the binarized images (second column) over 200 images and applying a Gaussian smoothing.

3. Results

This section starts with the validation of the LES by comparing predicted velocity field statistics to experimental measurements for case D_s, alongside a description of the main swirling flow features. The mixing behavior is then analyzed based on the computed helium mass fraction fields and the experimentally determined particle distributions. Next, the predicted hydrogen mass fraction fields from simulated case D are compared to the helium fields from D_s to assess the suitability of helium as a tracer for hydrogen macroscopic mixing. The effect of fuel composition on mixing quality is subsequently investigated both numerically and experimentally. Due to the significant differences observed between fuel compositions, the mixing process is further examined numerically through an analysis of the transport terms of the fuel mass fraction. Finally, the impact of fuel momentum injection on mixing quality is assessed experimentally.

3.1. Flow field analysis

Case D_s at J_{low} (surrogate case for $XH_2 = 1$) is first simulated numerically and the predicted velocity fields are compared to the experimentally measured flow field to validate the numerical model. Fig. 7 shows contour plots of axial (U) and transverse (V) velocity field in the mixing tube and combustion chamber, numerically predicted via LES and experimentally measured via PIV.

In agreement with experiments, the LES is capable to correctly predict the vortex breakdown at the transition from the mixing tube to the combustion chamber. As it enters the combustion chamber, the swirling flow forms a jet opening under the effect of the sudden cross section expansion and centrifugal forces.

The combined effect of adverse axial pressure gradient due to sudden cross section expansion and low pressure at the core, due to the swirling flow, induces the formation of a central recirculation zone (CRZ). At the considered swirl number conditions, the CRZ is not fully contained in the combustion chamber, but it is observed to form in the last section of the mixing tube, which could not be captured via PIV because of the baseplate. The LES predicts the location of the stagnation point at an axial location of $y \sim -5$ mm. Even if not optically accessible, the PIV flow field suggests that the stagnation point is located between $-10\,\text{mm} < y < -5\,\text{mm}$, coherently with the LES.

The axial and transverse velocity fields predicted by the LES show the presence of secondary flow patterns at the mixing tube core (see Fig. 7 LES). A wake region with almost zero axial velocity and intense inward radial velocity forms downstream of the central AAI duct at the swirler exit $y \sim -60$ mm, as the high velocity stream from the swirler vanes flows towards the mixing tube center to fill this low momentum region. The combined effect of radial velocity due to this wake region and the centrifugal force due to swirl gives origin to alternating regions

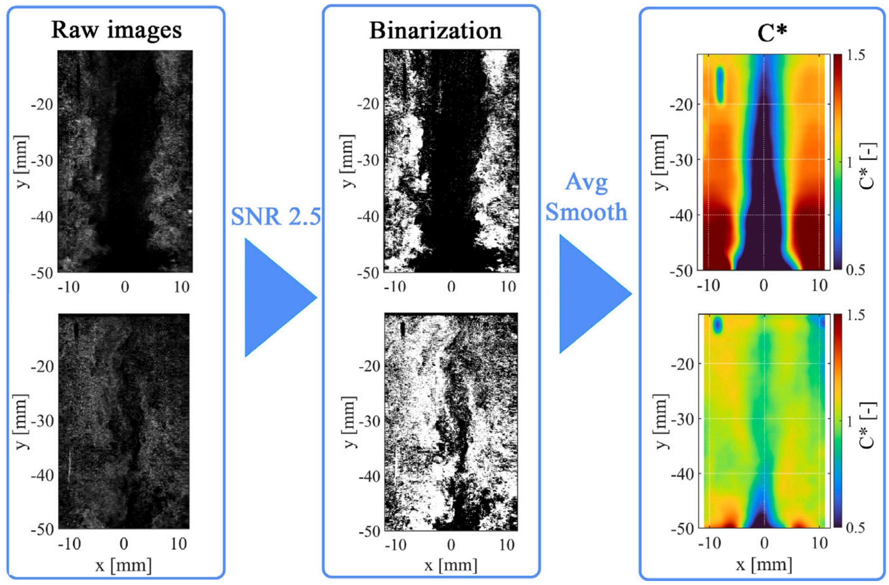

Fig. 6. Experimental methodology to determine particle concentration from raw Mie scattering images. From left to right, the process involves identifying the noise floor on background-subtracted images (first column), binarizing the image based on a signal-to-noise ratio (SNR) threshold of 2.5 (second column), and after averaging over 200 images and applying a Gaussian smoothing calculating the normalized particle concentration C^{*}. Examples illustrating a lower degree of premixing (top, case A_s, J_{low}) and a higher degree of premixing (bottom, case D_s, J_{high}).

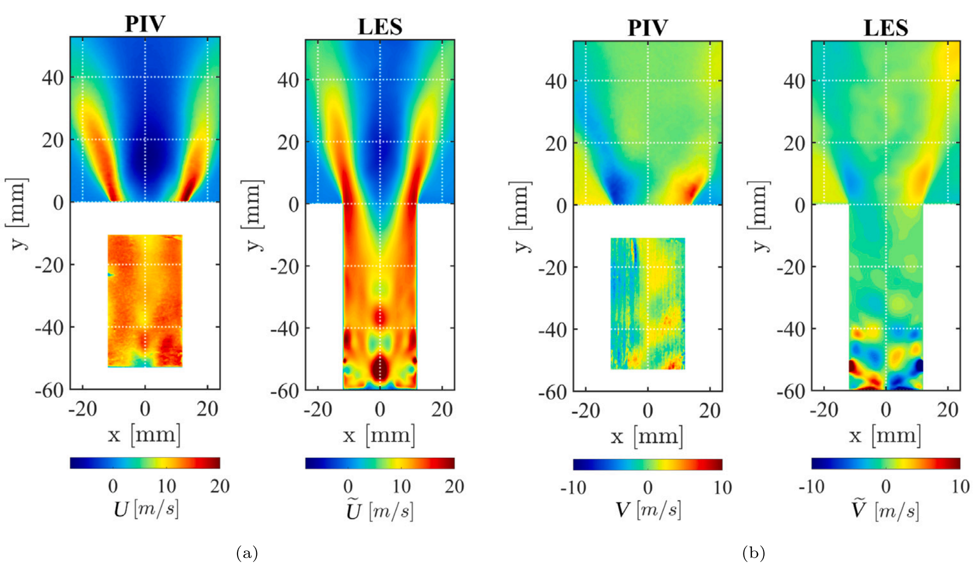

Fig. 7. Average streamwise velocity flow field (a) and average transverse velocity flow field (b) in the mixing tube and combustion chamber obtained experimentally by PIV (left) and numerically (right) for case D_s at J_{low}, Table 1.

of high and low axial and inward–outward radial velocity, identifying secondary recirculating structures. The same features can be qualitatively observed from PIV measurements, in particular the presence of low axial velocity at a location about $y \sim -50$ mm, and the alternating radial velocity pattern.

Numerically computed and experimentally measured radial profiles of average velocity in the combustion chamber are quantitatively compared in Fig. 8. A good prediction of the peak values in both the axial and transverse velocity components is observed. Close to the mixing tube outlet ($y = 8$ mm), the LES correctly predicts the peak axial velocity value within 9%, and the peak transversal velocity value within 6%. The jet opening is slightly underpredicted by the LES (LES = 22°, Exp 25°), as reflected in the prediction of the radial location of the velocity peaks for both components across all axial positions. Some asymmetry is noticed in the experimental values, which introduces discrepancies with numerical results on the right side of the observed window. The backflow velocity along the centerline is also well predicted by the LES, with an underestimation of its magnitude near the mixing tube exit at $y \sim 0$ mm. Higher-order statistics show good agreement, highlighting the LES's ability to predict turbulence intensity in the shear layers. The radial profile of the predicted axial velocity variance, $\overline{uu}$, qualitatively follows the distribution observed experimentally, with a correct prediction of the radial location of the peak values. Close to the mixing tube exit, $y = 2\,\text{mm} - 8\,\text{mm}$, the LES predicts the peak velocity within 20% accuracy, while further downstream the accuracy increases to 7%. For transverse velocity variance $\overline{vv}$, the LES correctly predicts the three-peaks radial profile observed experimentally at the mixing tube exit. The peak located on the centerline corresponds to the stagnation point upstream of the central recirculation zone and is underpredicted by the LES by 15%. Shortly downstream, $y = 8$ mm, the radial variance profile $\overline{vv}$ transitions to a two-peak shape, corresponding to the two branches

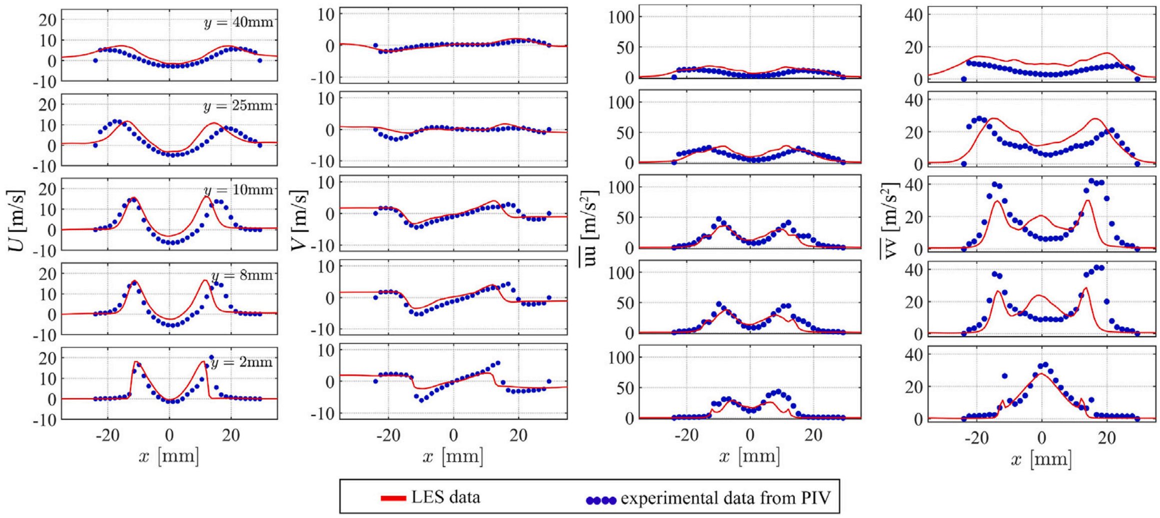

Fig. 8. From left to right: radial profiles of axial (U) and transverse (V) velocity and variance of axial ($\overline{uu}$) and transversal ($\overline{vv}$) fluctuating velocity components from LES (**—**) and experiments (•) at different streamwise locations y (rows).

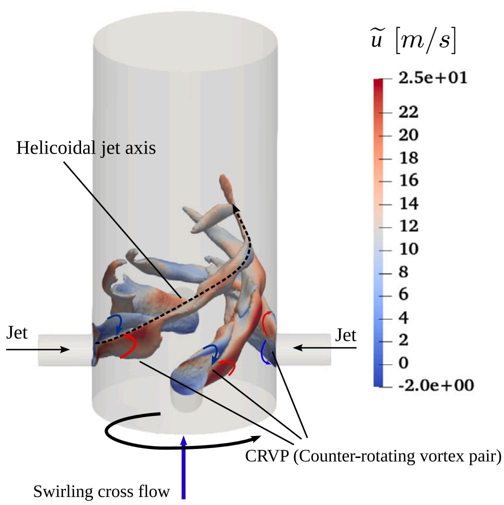

Fig. 9. Visualization of helium jets in swirling cross-flow structures in the mixing tube as predicted by LES of case D_s by instantaneous iso-surfaces of helium mass fraction Y_{He} = 0.25, colored by axial velocity $\tilde{u}$. (For interpretation of the references to color in this figure legend, the reader is referred to the web version of this article.)

of the opening jet. The LES correctly captures this shape from $y = 25$ mm on, but a peak on the centerline is still visible up to $y = 10$ mm, which is related to differences in the prediction of the CRZ axial location and jet opening angle.

Overall, the LES appears capable to capture the main flow features, including the vortex breakdown and the opening angle of the swirling jet, despite minor underpredictions in the peak velocity values.

3.2. Mixing process analysis

The fuel injection and mixing processes are investigated in this section. In Fig. 9 the development of the jet in swirling cross-flow structures is visualized through iso-surfaces of helium mass fraction as predicted by the LES for the same case D_s. The injected fuel stream is observed to follow a helical path as it mixes with the swirling flow. Interestingly, the positive and negative axial velocity values on the iso-surfaces reveal the presence of four counter-rotating vortex pairs, which consistently originate at the four fuel ports. These structures, formed by the pressure difference between the windward and leeward sides of the jet relative to the incoming swirling flow, are a characteristic feature of jets in cross-flow, as widely documented in the literature [33,49,50].

Fig. 10(a) shows the normalized fuel concentration C^* obtained from particle tracing in the helium fuel stream for the case D_s. The highest scattering intensity is observed at a location of $y \sim 50$ mm close to the fuel ports, where the fuel stream issues into the mixing tube and penetrates the swirling flow towards the centerline due to its radial injection momentum. The intensity magnitude and radial gradients of C^* clearly decrease in the streamwise direction as the fuel stream mixes with the swirling air stream. At the end of the experimental field of view ($y \sim -15$ mm), C^* drops to about 1 near the outer walls, while almost no particles are observed at the core, where C^* is still around 0.5. This stratification results from the combined effects of particle convection towards the center, driven by the radial injection momentum and associated to the jet in cross-flow development, and outward transport caused by centrifugal forces and radial velocity components, as analyzed in subsequent sections.

The time averaged field of helium mass fraction Y_{He} as predicted by the LES of case D_s is also reported in Fig. 10(b) and compared to C^* obtained from experiments. Coherently with what observed through particle tracking, high values of helium mass fraction are observed in correspondence of the fuel ports, with a decrease downstream as the helium jets spread and mix with the swirling cross-flow.

Closely downstream of the fuel ports, the numerical results reveal a pattern of isolated spots with high helium concentration, corresponding to the sectional view of the helical structures shown in Fig. 9. The same spots cannot be observed as clearly from experimental imaging in Fig. 10(a), possibly due to insufficient resolution to capture these patterns. On the other hand, this could suggest an under-prediction of turbulent mixing in the LES, and therefore a persistency of the coherent jet structures described in Fig. 9 up to an axial location of $y \sim -30$ mm (memory effect) [51,52]. In this regard, the LES predicts a weaker mixing than experimentally visualized in the first part of the mixing tube up to $y \sim -30$ mm. Downstream, stratification becomes more pronounced than in the LES, which may be due to the centrifugal separation effect. The particles tend to concentrate closer to the wall, having higher mass than the gas they track, for which instead a transport equation is solved in the LES.

As observed experimentally, a stratification of fuel is evident between the mixing tube wall and the central lean core. This region appears wider in the LES predictions compared to the experiment up to $y \sim -25$ mm. From $y \sim -20$ mm the central unmixed core exhibits a similar width in both the LES predictions and experimental measurements. The LES further predicts some mixture stratification at

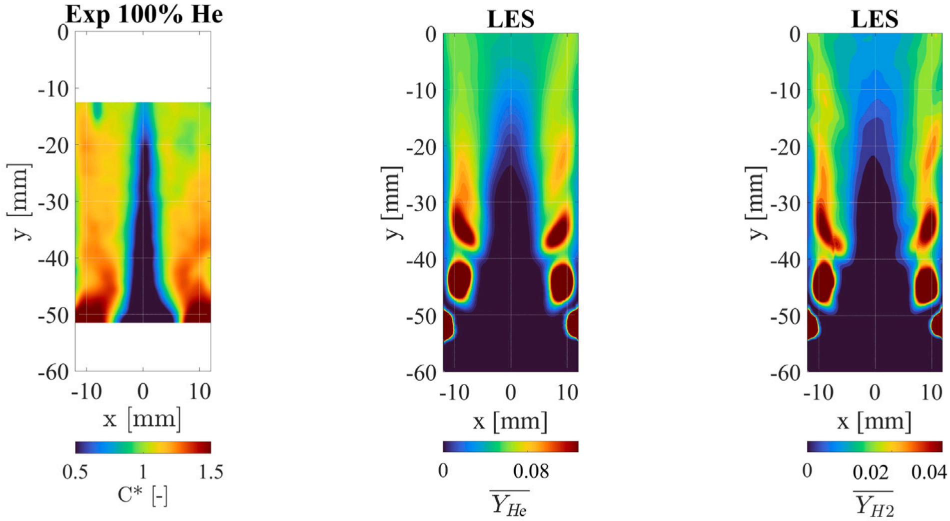

(a) (b) (c)

Fig. 10. (a) Experimentally obtained C^* of case D_s at J_{low}, (b) Helium mass fraction of case D_s at J_{low} (c) H_2 mass fraction of the reacting case D. (For interpretation of the references to color in this figure legend, the reader is referred to the web version of this article.)

the mixing tube exit, with helium mass fraction values of $Y_{He} \sim 0.04$ close to the wall and $Y_{He} \sim 0.0286$ at the mixing tube core, which are about 10% higher and 21% lower than the nominal value of 0.0362, respectively.

3.3. Suitability of He as a H_2 surrogate

The time-averaged H_2 mass fraction Y_{H_2} field, as predicted by the LES of case D, is also reported in Fig. 10(c) and compared to the helium mass fraction field from case D_s, in order to assess the suitability of Helium as a surrogate gas to predict the mixing behavior of H_2 in the present configuration. As already shown in Table 1, fuel ports in case D_s have larger diameter than case D, to achieve the same fuel jet momentum. The two cases display very similar mixing features, such as the fuel jet penetration and spread rate in the swirling cross-flow, the length of the lean core and mixture homogeneity at the mixing tube exit, where the H_2 mass fraction approaches its nominal value of 0.0184. Higher stratification is observed for H_2 in case D with respect to He in the surrogate case D_s towards the mixing tube exit. This results in higher mass fraction values than the nominal at the walls $Y_{H_2} \sim 0.022$ and 30% leaner than the nominal value at the core $Y_{H_2} \sim 0.013$. This suggests a slightly worse mixing of the H_2 case D as compared to the surrogate case D_s with helium.

A more quantitative description of mixing process and comparison of the two cases D and D_s is provided in Fig. 11 showing the radial profiles of time-averaged normalized mass fractions of the fuel agent C^* (left) and the RMS mass fraction values (right) at different axial locations. The pink lines represent case D (solid) and case D_s (dashed). Results are azimuthally averaged and plotted against the radial coordinate r. In the upstream part of the mixing tube $y = -52$ mm, the profiles illustrate the radial penetration of the fuel stream driven by the radial injection momentum. The RMS profiles shows a peak at a radial location $r \sim 8$–10 mm, corresponding to the region of steepest radial C^* gradients and identifying the mixing layer between the fuel stream and the incoming swirling air. At $y = -42$ mm, the normalized mass fraction value of both helium (case D_s) and hydrogen (case D) reaches a peak of approximately $C^* \sim 3$ at a radial location of $r = 9$ mm, marking the most inward fuel reach due to radial injection momentum. Further downstream, the profile spreads both inwards towards the mixing tube core and outward towards the wall as the fuel mixes downstream. The peak radial location shifts outwards, indicating fuel stratification towards the wall, while its magnitude decreases. Consistently, the RMS profiles display a double-peak structure from $y = -43$ mm downstream. The inner peak, higher in magnitude, corresponds to the intense mixing layer on the windward side of the fuel jet, where it interacts with the swirling air cross-flow. In contrast, the outer peak, which has a lower rms value, corresponds to the less intense mixing layer on the leeward side, where fuel spreads outward towards the wall. Eventually, the mass fraction profile tends to approach $C^* = 1$, as the mixture becomes homogeneous. Consequently, the RMS values diminish, and the double-peak structure transitions into a single peak, eventually flattening out.

The Helium mass fraction profiles in case D_s (pink dashed line) closely match the H_2 profiles of case D (pink solid line), especially close to the mixing tube exit. At these locations, case D shows slightly higher peaks of C^* than case D_s suggesting more stratification when using H_2, consistently with the contour plots in Fig. 10(c). At more upstream locations ($y = -36$ mm and $y = -52$ mm), higher He normalized mass fraction values with respect to H_2 are observed in a region between 5 and 9 mm from the centerline, suggesting a quicker penetration of helium towards the core of the swirling cross-flow, as confirmed by the higher RMS values of Y_{He} than Y_{H_2} at these locations. This is possibly associated to the overall slightly higher injection momentum of helium, as shown in Fig. 2(a), and may explain the ultimately more homogeneous mixture obtained for case D_s.

In summary, the LES results for case D_s demonstrate strong validation of the numerical model when compared to experimental data, showing accurate predictions of the velocity field and reasonable agreement in describing the mixing process. Furthermore, the numerical results from cases D and D_s confirm that helium serves as an effective surrogate for H_2 in replicating the mixing behavior under the present operating conditions, thereby supporting the validity of the experimental methodology. Building on this validation, the following section explores the impact of variations in fuel composition on mixing characteristics, maintaining constant operational power and air mass flow rate, through both numerical and experimental approaches.

3.4. Effect of fuel composition on fuel–air mixing

Fig. 12(a) presents the spatial unmixedness U_s (Eq. (7)) along the mixing tube for various surrogate fuel compositions, determined from post-processed Mie-scattering images of the J_{low} cases in Table 1. The spatial unmixedness, calculated using Eq. (7), is evaluated at multiple y-locations to assess mixture homogeneity and its streamwise evolution,

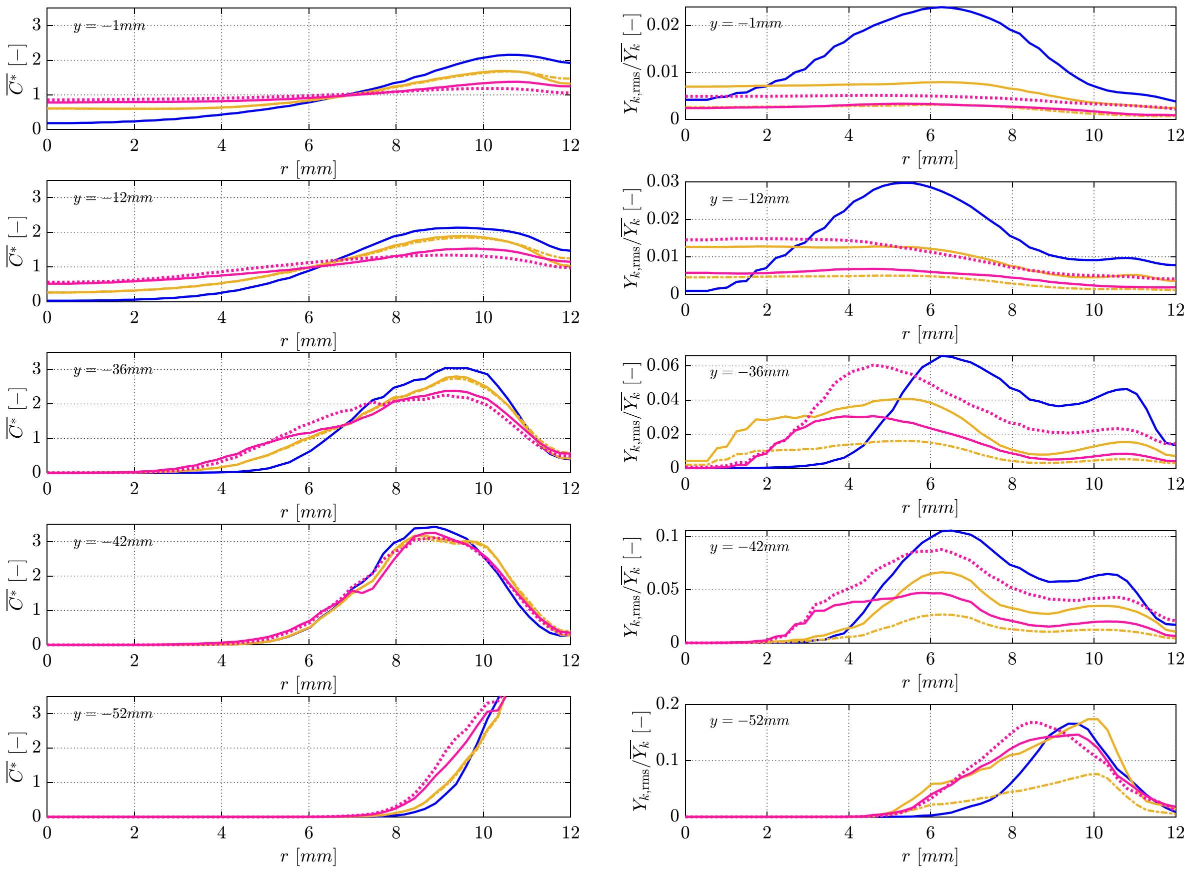

Fig. 11. Radial plots of time averaged normalized fuel mass distribution C^* (left) and fuel mass fraction temporal RMS normalized by its local time averaged value $Y_{k,rms}/\overline{Y_k}$ (right). LES results for case A $XH_2 = 0$, case C $XH_2 = 0.8$ (Y_{CH_4} and Y_{H_2}), case D $XH_2 = 1$ and surrogate case D_s. (For interpretation of the references to color in this figure legend, the reader is referred to the web version of this article.)

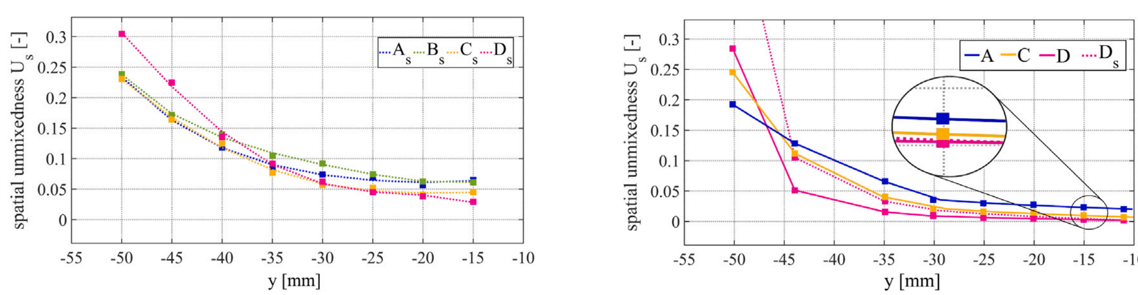

(a) (b)

Fig. 12. Spatial unmixedness at different y-locations for different fuel compositions and its surrogates at J_{low}: $XH_2 = 0$, $XH_2 = 0.4$, $XH_2 = 0.8$ an d $XH_2 = 1$ calculated from experimental data (a) and numerical data (b).

which reflects the rate of mixing. For cases A_s, B_s, and C_s representing CH_4/H_2 fuel mixtures of increasing H_2 content (0%, 40% and 80% H_2 in volume, respectively), the unmixedness at the most upstream location ($y = -50$ mm) consistently measures approximately $U_s \sim 0.24$. At $y = -15$ mm, a distinct correlation between higher helium content and better mixing quality is observed. At this location, cases A_s and B_s, representing a methane mass fraction above 90% in the fuel stream, yield nearly identical unmixedness values of $U_s \sim 0.055$, while case C_s (representing 66% methane by mass) achieves a slightly lower value of $U_s \sim 0.05$. In comparison, the full helium case (case D_s), which serves as a surrogate for pure H_2 fuel stream, exhibits the highest initial unmixedness value of $U_s \sim 0.3$ and experiences a more rapid mixing, with respect to the other tested fuel compositions, reaching the lowest unmixedness value $U_s \sim 0.025$ at the tube exit.

The same analysis is performed using LES (Fig. 12(b)), simulating the actual CH_4/H_2 fuel mixtures (cases A, C and D) alongside with the 100% helium case (case D_s). The simulations confirm the experimental findings, clearly highlighting that higher H_2 content in the fuel stream corresponds to higher upstream unmixedness, close the fuel injection ports, but it also promotes faster mixing along the tube, leading to a higher degree of mixing. This behavior may be attributed to a more inward penetration of the fuel stream towards the central core in the upstream regions, which increases unmixedness initially but accelerates mixing and enhances homogeneity further downstream. This is confirmed by the results in Fig. 11, where close to the fuel ports location $y = -50$ mm, higher H_2 content in the fuel mixtures results in higher C^* values closer to the mixing tube core ($r \sim$ 6–10 mm). Consistently, the inner RMS peak, which identifies the mixing layer, shows higher

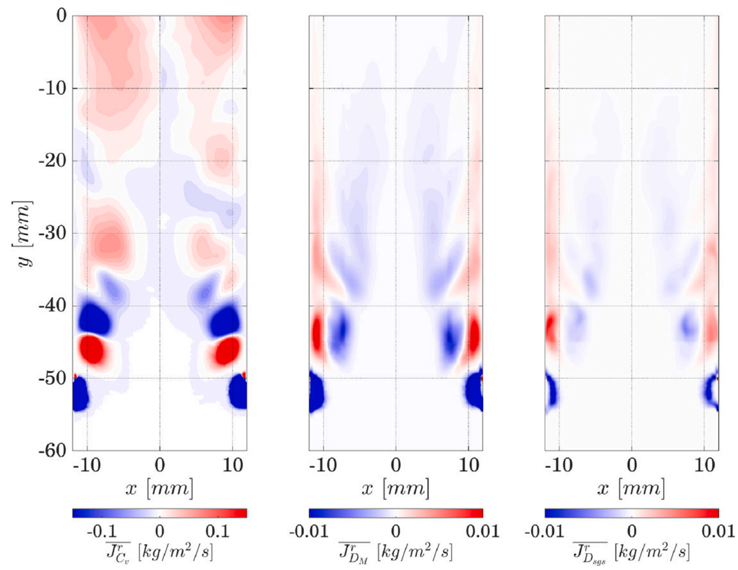

Fig. 13. Time averaged radial flux of Helium due to convective ($J^r_{C_v}$), molecular diffusive ($J^r_{D_M}$) and turbulent subgrid ($J^r_{D_{sgs}}$) transport as computed from the LES of case D_s.

values with increasing H_2 content and its radial location shifts closer to the mixing tube axis. Fuel penetration is primarily influenced by the initial fuel jet radial momentum and fuel diffusion. Moreover, in a swirled configuration, centrifugal forces act differently on two streams of different density, so that the air stream is pushed outwards more than the lighter fuel stream. This effect is more pronounced upstream in the mixing tube, where density gradients are stronger due to unmixedness, and it contributes to better mixing for lighter fuels. At the mixing tube exit, case A (100% methane) exhibits more significant fuel stratification, with a peak value $C^* \sim 2$, whereas case D shows a more homogeneous mixture with $C^* \sim 1$.

Both LES and experiments show that unmixedness decreases sharply between $y = -50$ mm and $y = -30$ mm, followed by an asymptotic trend downstream, suggesting that most of the mixing occurs in the upstream region of the mixing tube and residual unmixedness stratification persists further downstream. This is coherent with Fig. 11 where the C^* and RMS profile spread out between -52 mm to -36 mm while showing minimal changes downstream. Further mixing cannot occur due to balance between convective centrifugal transport and inward diffusion as further clarified by LES results in the next section. Therefore, when fixing the air mass flow rate and power setting, stratification appears inherent to the fuel properties and its injection momentum (which is constrained by the operating conditions in the considered geometry).

Despite the similarities between LES and experiments, LES predicts lower unmixedness values at the tube exit compared to experiments, suggesting better mixing performance for all investigated cases. This discrepancy arises from differences in measurement methods. While LES resolves the actual fuel gas distribution, experimental measurements rely on seeding the fuel stream with droplets. As mentioned Section 2.3, the discrepancies between LES and experimental data may be related to limitations of the DEHS droplets in representing the inertial and diffusive behavior of the gaseous fuel.

Nevertheless, both methods successfully capture the overarching trends, demonstrating that higher H_2 content consistently results in lower unmixedness values at the tube exit and that most of the mixing takes place in the first half of the mixing tube. To further explain the observed trends, a detailed analysis of radial fluxes in the transport equations is conducted next, followed by a comparative budget analysis of the transport terms across different fuel compositions (see Fig. 15).

3.5. Radial species fluxes

LES data in the mixing tube are further elaborated to provide a comprehensive overview of the mixing mechanisms in the present setup. To this scope, the helium case D_s is taken as a reference and the radial fluxes of helium mass fraction are computed. With reference to the filtered transport equation in Eq. (4), the radial fluxes are computed as:

$$J^r_{C_v} = \bar{\rho}\widetilde{u_r}\widetilde{Y_{He}} \qquad J^r_{D_M} = -\overline{\rho D^m_{He}\frac{\partial \widetilde{Y_{He}}}{\partial r}} \qquad J^r_{D_{sgs}} = -\frac{\mu_{sgs}}{Sc_t}\frac{\partial \widetilde{Y_{He}}}{\partial r}, \tag{9}$$

where convection $J^r_{C_v}$ is linked to the local helium mass fraction and radial velocity component values, while molecular diffusion $J^r_{D_M}$ and subgrid turbulent transport $J^r_{D_{sgs}}$ are driven by the mass fraction gradients. Fig. 13 reports the contour plots of the time averaged radial fluxes. The convective flux accounts for the majority of the transport near the fuel ports ($y = -52$ mm), where the initial jet momentum drives the fuel into the swirling flow up to a radial location of $x = 10$ mm. The secondary recirculating flow described in Fig. 7 and the characteristic helicoidal fuel stream structures with counter-rotating vortex pair (Fig. 9) give origin to peculiar alternating inward and outward convective flux patterns. The radial velocity component is quickly redirected by the incoming swirled cross-flow into stronger streamwise and tangential components, as the flow in the mixing tube transitions to a homogeneously swirling state (Fig. 7). Consequently, the convective flux decreases to a value below 0.05 at an axial location around $y \sim -35$ mm, and the inward (negative) convective flux fades. Further downstream, the inward component is almost completely suppressed along with the weakening of secondary recirculation zones (Fig. 7), leaving a residual outward flux from $y = -30$ mm downstream. This outward flux intensifies near the outlet, as the mixture must flow around the central recirculation zone located close to the mixing tube outlet, Fig. 7.

Analyzing the diffusion fluxes reveals that the molecular diffusion intensity is comparable to that of turbulent diffusion (in the case of helium), emphasizing the importance of accurately modeling molecular diffusion. At most locations (e.g. $y > -50$ mm), the turbulent diffusion value is even smaller than the molecular diffusion, suggesting good mesh resolution and low turbulence level due to the very low Reynolds numbers of the fuel stream ($Re \approx 800$). The diffusion flux patterns follow mass fraction gradients, with the strongest intensity occurring in the shear layer. In particular, negative diffusive flux (inwards) is observed towards inner radial regions, in correspondence of the windward mixing layer between fuel jet and cross-flow, previously

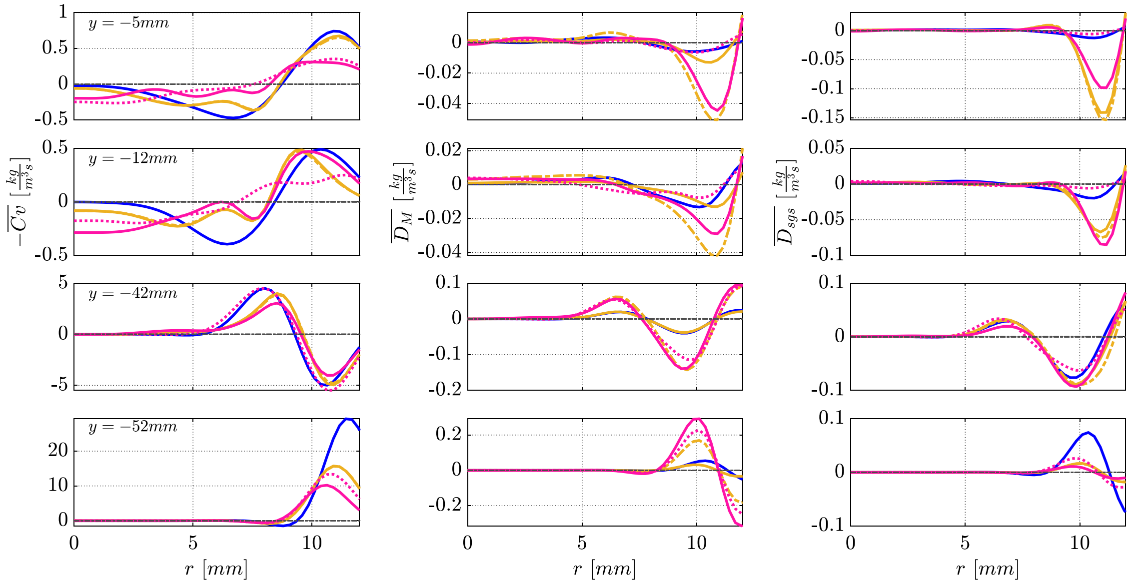

Fig. 14. Radial profiles of the transport terms in the radial direction for the fuel mass fraction according to Eq. (11) for case A $XH_2 = 0$ (—), case C $XH_2 = 0.8$ (Y_{CH_4} (—) and Y_{H_2} (- -)), case D $XH_2 = 1$ (—) and surrogate case D_s (⋯). (For interpretation of the references to color in this figure legend, the reader is referred to the web version of this article.)

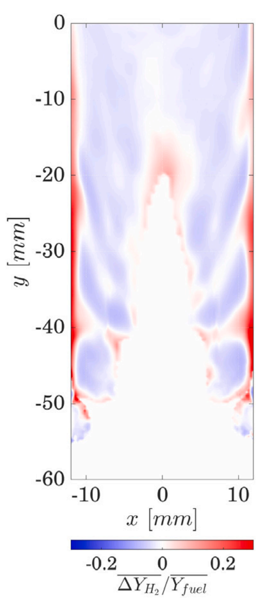

Fig. 15. Local variation of H_2 mass fraction in the fuel composition at a random time for case C.

identified in Fig. 11 with the inner RMS peak and maximum mass fraction gradient. Analogously, at a streamwise location of $y \sim -45$ mm, positive diffusive flux, spreading fuel towards the outer boundary layer is observed, which is associated with the leeward mixing layer. Consistently with previous observations, most of the mixing appears to occur upstream of $y = -30$ mm, where convection and diffusion fluxes remain strong due to residual radial velocity components (from fuel injection or recirculation) and significant fuel mass fraction gradients are present. Downstream of $y = -30$ mm, these gradients smooth out (as seen in Fig. 11) and the inward radial momentum dissipates, resulting in significantly milder mixing. At these locations, the primary factor contributing to the described fuel stratification is the predominance of outward convection (driven by the presence of the central recirculation zone at the mixing tube exit), while diffusion diminishes due to the mitigated mass fraction gradients associated to the increasingly homogeneous mixture.

3.6. Radial transport budget analysis

Next, a budget analysis is carried out to evaluate the strength of transport terms for different fuel compositions and compare them. Considering the time-averaged form of Eq. (4), and assuming the time derivative is zero due to steady-state flow, the transport terms given by the local divergence of species fluxes ($-\nabla \cdot J_k$) must balance, such that:

$$-C_{v,k} + D_{M,k} + D_{sgs,k} = 0, \tag{10}$$

being $-C_{v,k}$, $D_{M,k}$ and $D_{sgs,k}$ the species k transport terms appearing in Eq. (4) associated to convection, molecular and subgrid transport, respectively. Considering only the radial contribution of the three radial fluxes to the transport budget of a species k, these terms are computed as follows:

$$C^r_{v,k} = \frac{\partial}{\partial r}\left(\bar{\rho}\widetilde{u_r}\widetilde{Y_{He}}\right) \qquad D^r_{M,k} = \frac{\partial}{\partial r}\left(\overline{\rho D^m_{He}\frac{\partial \widetilde{Y_{He}}}{\partial r}}\right)$$

$$D^r_{sgs,k} = \frac{\partial}{\partial r}\left(\frac{\mu_{sgs}}{Sc_t}\frac{\partial \widetilde{Y_{He}}}{\partial r}\right) \tag{11}$$

The time averaged radial profiles of the budget terms in Eq. (11) are reported in Fig. 14 for different streamwise locations. These terms are normalized by the spatial average of the fuel mass fraction at each y-location to express the transport terms relative to C^*, thereby highlighting the relative significance of each term with respect to the local level of unmixedness. Negative values of the budget term indicate that convection or diffusion are transporting fuel away from a specific radial location, whereas positive values represent transport towards that location.

Consistently with Fig. 13, at the fuel port exit, convection accounts for most of the radial transport since the fuel is injected into the mixing tube with its initial radial momentum. Case A (blue line) exhibits the highest peak value of the convective transport term due to the higher mass flow rate of methane compared to the other cases (see blue line, left column last row in Fig. 14). However, cases with higher H_2 content (yellow line C and pink line D) exhibit a further fuel entry towards the center of the mixing tube, as indicated by a more inward peak location in the convection profile and a wider distribution of nonzero values extending further inwards. This behavior, consistent with the trends described earlier (Figs. 11–12(b)), is associated with the higher fuel momentum in these cases.

Further downstream, at $y = -42$ mm, the convection term continues to transport fuel radially inwards for all the cases, from $r = 4$ mm (peak of negative budget value) to $r = 8$–9 mm (peak of positive budget value). As expected, the convection term has lower values here than at the fuel ports, where the radial velocity due to the injection is at its maximum. At this downstream location, convection is primarily driven by radial velocity induced by the secondary recirculations described earlier (Fig. 7).

The diffusive transport (both molecular and turbulent) displays a double-peak profile (middle and right column in Fig. 14), indicating fuel transport via diffusion from $r \sim 9$–10 mm (where the maximum fuel mass fraction appears, as shown in Figs. 11 and 10) both towards the mixing tube core (up to $r = 4$ mm) and outwards into the boundary layer, as previously described. Although diffusive transport is two orders of magnitude weaker than convection, it still promotes fuel transport towards the center at each streamwise location. Notably, in cases C and D, the molecular diffusion of H_2 has similar magnitudes as turbulent diffusion, and between $r = 4$ mm and $r = 6$ mm, it becomes comparable to convection.

Towards the mixing tube exit ($y = -12$ mm and $y = -5$ mm), the intensity of convection is drastically reduced by an order of magnitude for all the cases. Here, radial transport is primarily driven by outward radial velocity associated with vortex breakup and the presence of the central recirculation zone (CRZ) at the tube exit (Fig. 7). At this location, convection appears to promote stratification, while diffusion opposes it. In facts, H_2 and helium (cases D and D_s) are less subject to outward radial convection as compared to methane and CH_4/H_2 mixtures (case A and C) due to their lower density, while their molecular diffusion remains significant, ultimately displaying the lowest levels of unmixedness and stratification.

Interestingly, Fig. 14 demonstrates how the species in a multicomponent fuel are subject to different transport mechanisms. Specifically, in case C ($XH_2 = 0.8$), hydrogen's diffusive transport (yellow dashed line) exhibits peak values approximately 50% higher than methane's diffusive transport (yellow solid line). Conversely, convective and turbulent diffusion transport are nearly identical for the two species. The effects of these differences in diffusivity are illustrated in Fig. 15, which shows the local drift in the hydrogen-to-fuel mass fraction ratio relative to its nominal value at injection, thereby highlighting the H_2/CH_4 separation within the fuel mixture. Hydrogen diffuses more significantly than methane across the upwind and leeward mixing layers, both reaching deeper into inner mixing tube core and forming a hydrogen-rich zone (red values) at the boundary layer, where molecular diffusion dominates over turbulence.

3.7. Effect of J_{swirl} on the fuel–air mixing

The previous sections examined the effect of varying fuel compositions on mixing characteristics. The budget analysis of the transport terms showed that the convective term contributes most significantly to mixing, particularly just downstream of the fuel injection ports. This suggests that the majority of mixing occurs near the injection points. Consequently, this section explores the impact of varying the value of J_{swirl} to enhance mixing. Additionally, it assesses the influence of fuel composition or J_{swirl} on the mixing process.

Fig. 16 shows, on the left-hand side, the spatial unmixedness (U_s) for various jet to cross-flow momentum ratios (J_{swirl} defined in section combination experimental & numerical design, Fig. 2(a)) at different streamwise locations for the 100% H_2 surrogate (case D_s). The graph clearly shows that close to the fuel injection point ($y = -50$ mm) the value for U_s decreases as J_{swirl} increases. This trend is intuitive because higher values of J_{swirl} correspond to deeper jet penetration into the swirling flow, allowing more helium to reach the centerline of the flow. This behavior is also evident in the contour plots of the normalized fuel distribution C^* (Fig. 16, right-hand side). These two contour plots zoom in the region between $y = -50$ mm and $y = -40$ mm, for $J_{\mathrm{swirl}} = 0.24$ (which corresponds to the base case analyzed in Fig. 10(a)) and $J_{\mathrm{swirl}} = 9.9$. At $y = -45$ mm, the dark blue region, representing areas with few or no particles, narrows significantly as J_{swirl} increases. For $J_{\mathrm{swirl}} = 9.9$, the value for U_s drops below 0.1 upstream of $y = -40$ mm, and remains nearly constant throughout the field of view in the mixing tube (till $y = -15$ mm). This is reflected in the contour plot, where the particle distribution for $J_{\mathrm{swirl}} = 9.9$ appears nearly uniform by $y = -40$ mm. In contrast, for $J_{\mathrm{swirl}} = 4.85$, U_s decreases more gradually, reaching a similar value to $J_{\mathrm{swirl}} = 9.9$ at $y = -20$ mm. This behavior suggests that, as discussed previously in Fig. 14, mixing near the injection point is primarily driven by convection, which is weaker at lower J_{swirl}. However, the mixing tube is long enough to ensure a low unmixedness value even if J_{swirl} is reduced to $J_{\mathrm{swirl}} = 4.85$. For the lowest investigated J_{swirl}, the initial level of unmixedness is considerably higher compared to the higher J_{swirl} values. Nevertheless, as the flow progresses through the mixing tube, the unmixedness steadily decreases. While it approaches the levels observed for higher J_{swirl} values, it does not achieve the same degree of uniformity within the field of view. This suggests that for the lowest J_{swirl}, a longer mixing tube would be required to reach the same unmixedness level as for the higher J_{swirl} values.

Fig. 17 presents the experimental results for the spatial unmixedness values and the normalized fuel concentration C^* for a lower H_2 content surrogate (case B_s, $XH_2 = 0.4$). Interestingly, the case with a higher momentum flux ratio ($J_{\mathrm{swirl}} = 6.8$) exhibits greater unmixedness in the upstream region of the field ($y = -50$ mm). This is likely due to the pronounced asymmetry observed in the case with a lower J_{swirl} ($J_{\mathrm{swirl}} = 0.17$), as reflected in the contour plot for C^*. Focusing on the range $-11\,\mathrm{mm} < x < 0\,\mathrm{mm}$, C^* for $J_{\mathrm{swirl}} = 6.8$ shows a higher penetration depth, evident from the region of high particle density (dark red areas). Additionally, the length of these red regions in the streamwise direction is reduced for the higher J_{swirl}, suggesting that the mixing process occurs more rapidly. Further downstream (beyond $y = -30$ mm), the unmixedness value for the case with higher J_{swirl} is lower than that for lower J_{swirl}, indicating that the mixture enters the combustion chamber at a higher degree of mixing. This observation aligns with the trends shown in Fig. 16. Comparing Figs. 16 and 17 it is evident that unmixedness is lower for all investigated J_{swirl} in case D_s compared to B_s close to the mixing tube outlet. This indicates that the fuel composition has a more significant effect on the mixing performance than J_{swirl}. As previously mentioned in Section 3.5, a fuel stream lighter than air experiences lower centrifugal forces than the swirling air stream, which, in this configuration, promotes better mixing and allows the fuel to more easily reach the core. Furthermore, as analyzed in the previous section, helium (or H_2) are less affected by outward radial convection at the mixing tube outlet than methane (or its surrogate gas) due to their lower density, resulting in reduced stratification. Additionally, helium exhibits higher inward diffusive transport due to its greater molecular diffusivity.

4. Conclusions

The present study proposes a combined experimental and numerical approach to investigate the mixing behavior of a jet in swirling cross-flow configuration, representative of a lab-scale injector of a partially-premixed, swirl-stabilized burner. Mie scattering images of the seeded fuel stream enable particle count techniques to evaluate the degree of mixing, while Large Eddy simulations (LES) solving species transport equations are used to study the problem numerically. The study focuses on the influence of fuel composition and jet to cross-flow momentum flux ratio J_{swirl} on the mixing process. Mixing performance is evaluated using a spatial unmixedness parameter U_s, and by examining the radial profiles of species mass fractions obtained from numerical simulations. To represent CH_4/H_2 fuel mixtures, helium/air

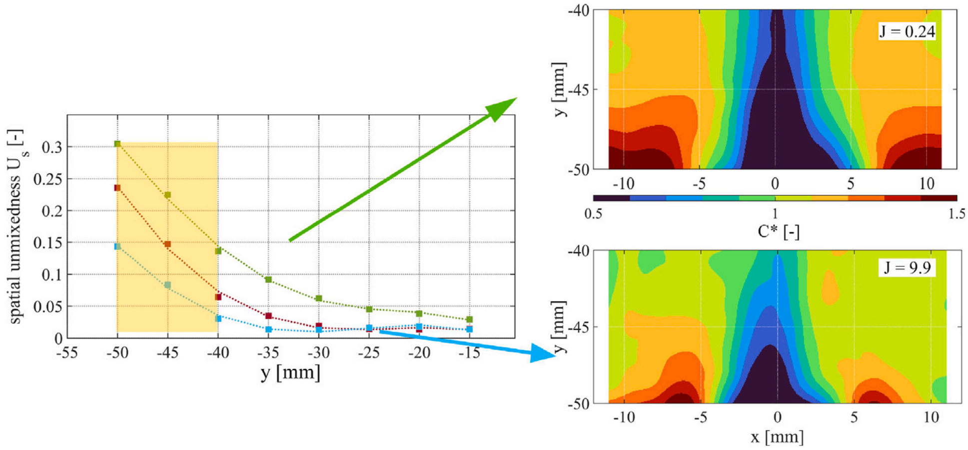

Fig. 16. Left side: Spatial unmixedness obtained from normalized Mie scattering Images for D_s (XH_2 = 1) at different levels of J_{swirl}, J_{swirl} = 0.23 (····), J_{swirl} = 4.85 (····) and J_{swirl} = 9.9 (····). Right side: Level of C^* for J_{swirl} = 0.23 and J_{swirl} = 9.9, field of view indicated in yellow in the graph. (For interpretation of the references to color in this figure legend, the reader is referred to the web version of this article.)

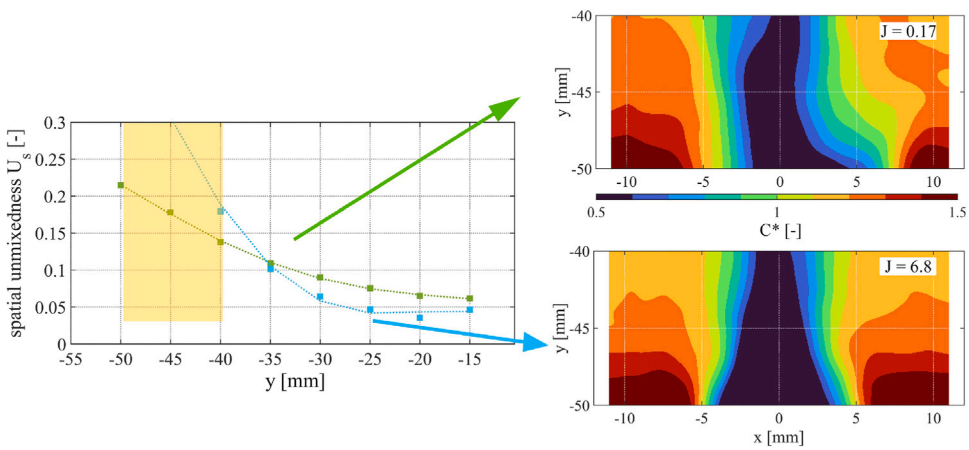

Fig. 17. Left side: Spatial unmixedness obtained from normalized Mie scattering images for B_s (XH_2 = 0.4) at different levels of J_{swirl}, J_{swirl} = 0.17 (····), and J_{swirl} = 6.8 (····). Right side: Level of C^* for J_{swirl} = 0.23 and J_{swirl} = 9.9, field of view indicated in yellow in the graph. (For interpretation of the references to color in this figure legend, the reader is referred to the web version of this article.)

mixtures with varying helium concentrations are employed, with the suitability of helium as a surrogate for H_2 validated through numerical simulations. The key conclusions are as follows:

1. Helium is validated as a reliable surrogate for hydrogen for assessing macroscopic fuel–air mixing trends in partially premixed swirl-stabilized injectors. A suitable strategy to use helium is to keep the momentum flux ratio J_{swirl} constant. Due to the higher helium density, equal jet momentum (at constant mass flow rate) has to be achieved by adjusting the fuel inlet diameter.
2. In fuel blends of CH_4 and H_2, the higher diffusivity of H_2 into air with respect to CH_4 can result in a H_2 rich region at the mixing tube wall near the entrance in the combustion chamber, exacerbating potential criticalities related to boundary layer flashback.
3. For similar values of J_{swirl}, decreasing the density of the fuel stream improves mixing. Convection dominates mixing near the injection ports, but it drives outward fuel stratification downstream, near the mixing tube exit. In contrast, molecular diffusion transports fuel species across the jet's windward and leeward shear layers, enhancing mixing towards the mixing tube center at all streamwise locations. H_2 and He undergo less downstream stratification because of their lower density and higher molecular diffusivity compared to CH_4, both improving mixing.
4. The fuel density has a more significant influence on the degree of mixing than the level of J_{swirl}. This is due to the fact that lighter fuels are less subject to outward convection, therefore less prone to stratification, and their higher diffusivity promotes their mixing towards the central core.
5. A higher value for J_{swirl} results in a higher penetration depth of the jet into the cross-flow, which decreases the initial level of unmixedness. The results indicate, that a critical J_{swirl} value exists beyond which, at any given mixing tube length, the final unmixedness level is insensitive to fuel injection momentum J_{swirl}.

5. Outlook & considerations

The non-reacting results indicate that increasing the H_2 content improves mixing in fuel-flexible (CH_4/H_2) combustion systems with a jet in cross-flow configuration. Enhanced mixing with higher H_2 content could contribute to reduced NO_x emissions, assuming constant adiabatic flame temperature, by lowering the operating equivalence ratio. However, due to hydrogen's significantly higher flame speed, the flame may anchor further upstream in regions where the fuel and air are less premixed, potentially increasing NO_x levels. As such, direct estimation of NO_x from non-reacting mixing data alone is challenging.

An increase in J_{swirl} improves mixing across all H_2 fractions, which could favor reduced NO_x emissions. However, a critical J_{swirl} value was identified, beyond which further increases no longer significantly enhance mixing. This finding is particularly relevant for reacting conditions, as it suggests the existence of an optimal mixing tube length, beyond which further extension offers no mixing benefit and may increase the risk of flashback in H_2-rich flames.

While non-reacting studies provide valuable trends, they may not fully capture the behavior under reacting conditions. Nevertheless, they offer useful insights into mixing characteristics and flame anchoring behavior. Future work will focus on validating these non-reacting findings under reacting conditions, specifically examining whether changes in mixing degree correlate with NO_x emissions and how fuel distribution affects flashback limits.

CRediT authorship contribution statement

Sarah Link: Writing – review & editing, Writing – original draft, Visualization, Methodology, Investigation, Conceptualization. **Gioele Ferrante:** Writing – review & editing, Writing – original draft, Visualization, Methodology, Investigation, Conceptualization. **Kaushal Dave:** Writing – review & editing, Methodology. **Giulia Monti:** Writing – review & editing, Methodology, Investigation, Conceptualization. **Georg Eitelberg:** Writing – review & editing, Supervision. **Francesca de Domenico:** Writing – review & editing, Supervision, Methodology, Investigation, Conceptualization.

Declaration of competing interest

The authors declare the following financial interests/personal relationships which may be considered as potential competing interests: Sarah Link and Gioele Ferrante report financial support was provided by Safran Tech. If there are other authors, they declare that they have no known competing financial interests or personal relationships that could have appeared to influence the work reported in this paper.

Acknowledgments

This project has been financed by the Dutch Ministry of Economic Affairs and Climate under the TKIscheme (Grant number TKI HTSM/18.0170) along with SAFRAN TECH.

We acknowledge EuroHPC JU for awarding the project ID EHPC-REG-2024R01-064 access to MeluXina CPU in Luxembourg. The work is carried out in the framework of the Regular Access project FULCRUMS (high-Fidelity cfd simULations of non-Conventional hydRogen combUstion systeM for aeronauticS). The authors gratefully acknowledge the LuxProvide teams for their expert support.

The authors further acknowledge the use of the Dutch National Supercomputer Snellius with the support of the SURF Cooperative using grant no. [EINF-8010] to perform the simulations reported in the present work.

References

[1] Hoelzen J, Silberhorn D, Zill T, Bensmann B, Hanke-Rauschenbach R. Hydrogen-powered aviation and its reliance on green hydrogen infrastructure – review and research gaps. Int J Hydrog Energy 2022;47(5):3108–30. http://dx.doi.org/10.1016/j.ijhydene.2021.10.239, Hydrogen Energy and Fuel Cells.

[2] York WD, Ziminsky WS, Yilmaz E. Development and Testing of a Low NOx Hydrogen Combustion System for Heavy-Duty Gas Turbines. J Eng Gas Turbines Power 2013;135(2):022001. http://dx.doi.org/10.1115/1.4007733.

[3] Ma N, Zhao W, Wang W, Li X, Zhou H. Large scale of green hydrogen storage: Opportunities and challenges. Int J Hydrog Energy 2024;50:379–96. http://dx.doi.org/10.1016/j.ijhydene.2023.09.021.

[4] Tao M, Azzolini JA, Stechel EB, Ayers KE, Valdez TI. Review—Engineering challenges in green hydrogen production systems. J Electrochem Soc 2022;169(5):054503. http://dx.doi.org/10.1149/1945-7111/ac6983.

[5] Sommerer Y, Galley D, Poinsot T, Ducruix S, Lacas F, Veynante D. Large eddy simulation and experimental study of flashback and blow-off in a lean partially premixed swirled burner. J Turbul 2004;5(1):037. http://dx.doi.org/10.1088/1468-5248/5/1/037.

[6] Tao C, Zhou H. Effect of hydrogen blending on thermoacoustic instability and flashback dynamics in partially premixed methane-air flames. Fuel 2025;393:135007. http://dx.doi.org/10.1016/j.fuel.2025.135007.

[7] Allison PM, Driscoll JF, Ihme M. Acoustic characterization of a partially-premixed gas turbine model combustor: Syngas and hydrocarbon fuel comparisons. Proc Combust Inst 2013;34(2):3145–53. http://dx.doi.org/10.1016/j.proci.2012.06.157.

[8] Marragou S, Magnes H, Poinsot T, Selle L, Schuller T. Stabilization regimes and pollutant emissions from a dual fuel CH4/H2 and dual swirl low NOx burner. Int J Hydrog Energy 2022;47(44):19275–88. http://dx.doi.org/10.1016/j.ijhydene.2022.04.033.

[9] Marragou S, Magnes H, Aniello A, Selle L, Poinsot T, Schuller T. Experimental analysis and theoretical lift-off criterion for H2/air flames stabilized on a dual swirl injector. Proc Combust Inst 2023;39(4):4345–54. http://dx.doi.org/10.1016/j.proci.2022.07.255.

[10] Marek C, Smith T, Kundu K. Low emission hydrogen combustors for gas turbines using lean direct injection. In: 41st AIAA/aSME/SAE/ASEE joint propulsion conference and exhibition. 2005, http://dx.doi.org/10.2514/6.2005-3776.

[11] Reichel TG, Terhaar S, Paschereit CO. Flashback resistance and fuel–air mixing in lean premixed hydrogen combustion. J Propuls Power 2018;34(3):690–701. http://dx.doi.org/10.2514/1.B36646.

[12] Bai N, Fan W, Zhang R. A mixing enhancement mechanism for a hydrogen transverse jet coupled with a shear layer for gas turbine combustion. Phys Fluids 2023;35(4). http://dx.doi.org/10.1063/5.0142960.

[13] Karagozian AR. The jet in crossflow. Phys Fluids 2014;26(10). http://dx.doi.org/10.1063/1.4895900.

[14] Margason RJ. Fifty years of jet in cross flow research. In AGARD, Comput Exp Assess Jets Cross Flow 1993.

[15] Mahesh K. The interaction of jets with crossflow. Annu Rev Fluid Mech 2013;45:379–407. http://dx.doi.org/10.1146/annurev-fluid-120710-101115.

[16] Majander P, Siikonen T. Large-eddy simulation of a round jet in a cross-flow. Int J Heat Fluid Flow 2006;27(3):402–15. http://dx.doi.org/10.1016/j.ijheatfluidflow.2006.01.004.

[17] Cortelezzi L, Karagozian AR. On the formation of the counter-rotating vortex pair in transverse jets. J Fluid Mech 2001;446:347–73. http://dx.doi.org/10.1017/S0022112001005894.

[18] Salewski M, Stankovic D, Fuchs L. Mixing in circular and non-circular jets in crossflow. Flow Turbul Combust 2008;80:255–83. http://dx.doi.org/10.1007/s10494-007-9119-x.

[19] Liscinsky D, True B, Holdeman J. Crossflow mixing of noncircular jets. J Propuls Power 1995;12. http://dx.doi.org/10.2514/3.24017.

[20] Wegner B, Huai Y, Sadiki A. Comparative study of turbulent mixing in jet in cross-flow configurations using LES. Int J Heat Fluid Flow 2004;25(5):767–75. http://dx.doi.org/10.1016/j.ijheatfluidflow.2004.05.015, Selected papers from the 4th International Symposium on Turbulence Heat and Mass Transfer.

[21] Schetz JA, Harsha PT. Injection and Mixing in Turbulent Flow (Progress in Aeronautics and Astronautics, Vol. 68). J Fluids Eng 1980;102(4). http://dx.doi.org/10.1115/1.3240750, 525–525.

[22] Crabb D, Durão DFG, Whitelaw JH. A round jet normal to a crossflow. J Fluids Engineering- Trans the Asme 1981;103:142–53. http://dx.doi.org/10.1115/1.3240764.

[23] Holdeman JD. Mixing of multiple jets with a confined subsonic crossflow. Prog Energy Combust Sci 1993;19(1):31–70. http://dx.doi.org/10.1016/0360-1285(93)90021-6.

[24] Kandakure MT, Patkar VC, Patwardhan AW, Patwardhan JA. Mixing with jets in cross-flow. Ind Eng Chem Res 2009;48(14):6820–9. http://dx.doi.org/10.1021/ie801863a.

[25] Li Z, Murugappan S, Gutmark E, Vallet L. Numerical simulation and experiments of jets in cross flow. In: Collection of technical papers - 44th AIAA aerospace sciences meeting. Vol. 6, 2006, http://dx.doi.org/10.2514/6.2006-307.

[26] Bons JP, Sondergaard R, Rivir RB. The Fluid Dynamics of LPT Blade Separation Control Using Pulsed Jets . J Turbomach 2001;124(1):77–85. http://dx.doi.org/10.1115/1.1425392.

[27] Bilger W, Dibble RW. Differential molecular diffusion effects in turbulent mixing. Combust Sci Technol 1982;28(3–4):161–72. http://dx.doi.org/10.1080/00102208208952552.

[28] Syred N, Chigier N, Beér J. Flame stabilization in recirculation zones of jets with swirl. Symp (International) Combust 1971;13(1):617–24. http://dx.doi.org/10.1016/S0082-0784(71)80063-2, Thirteenth symposium (International) on Combustion.

[29] Kruljevic B, Darabiha N, Durox D, Vaysse N, Renaud A, Vicquelin R, Fiorina B. Experimentation and simulation of a swirled burner featuring cross-flow hydrogen injection with a focus on the oh* chemiluminescence. Combust Flame 2025;273:113945. http://dx.doi.org/10.1016/j.combustflame.2024.113945.

[30] Syred N, Beér JM. Combustion in swirling flows: A review. Combust Flame 1974;23(2):143–201. http://dx.doi.org/10.1016/0010-2180(74)90057-1.

[31] Ahmed S, So R. Characteristics of air jets discharging normally into a swirling crossflow. AIAA J 1987;25:429–35. http://dx.doi.org/10.2514/3.9641.

[32] So R, Ahmed S. Helium jets discharging normally into a swirling air flow. Exp Fluids 1987;5(4):255–62. http://dx.doi.org/10.1007/BF00279739.

[33] Tan T, Fan W, Zhang R. A numerical and experimental investigation into the mixing mechanism of hydrogen transverse jets into an air swirl flow. Phys Fluids 2024;36(3):037147. http://dx.doi.org/10.1063/5.0198960.

[34] Link S, Dave K, de Domenico F, Rao AG, Eitelberg G. Experimental analysis of dual-fuel (CH4/H2) capability in a partially-premixed swirl stabilized combustor. Int J Hydrog Energy 2025;101:427–37. http://dx.doi.org/10.1016/j.ijhydene.2024.12.286.

[35] Ferrante G, Doodeman L, Rao AG, Langella I. LES of Hydrogen-Enriched Methane Flames in a Lean-Burn Combustor With Axial Air Injection. In: Turbo expo: power for land, sea, and air. Volume 3B: Combustion, Fuels, and Emissions, 2023, V03BT04A015. http://dx.doi.org/10.1115/GT2023-103006.

[36] Beér J, Chigier N. Combustion aerodynamics [by] j.m. Beér and n.a. Chigier. Fuel and energy science series, Applied Science Publishers Limited; 1972.

[37] Oamjee A, Sadanandan R. Suitability of helium gas as surrogate fuel for hydrogen in H2-air non-reactive supersonic mixing studies. Int J Hydrog Energy 2022;47(15):9408–21. http://dx.doi.org/10.1016/j.ijhydene.2022.01.022.

[38] Tropea C, Yarin A, Foss J. Springer Handbook of Experimental Fluid Mechanics. Springer; 2007, http://dx.doi.org/10.1007/978-3-540-30299-5.

[39] Pope SB. Turbulent flows. Meas Sci Technol 2001;12(11). http://dx.doi.org/10.1088/0957-0233/12/11/705.

[40] Chemical-kinetic mechanisms for combustion applications. In: San Diego Mechanism web page, Mechanical and Aerospace Engineering (Combustion Research). University of California at San Diego, URL http://combustion.ucsd.edu.

[41] Yoshizawa A. Statistical theory for compressible turbulent shear flows, with the application to subgrid modeling. Phys Fluids 1986;29(7):2152–64. http://dx.doi.org/10.1063/1.865552.

[42] Williams FA. Combustion theory. CRC Press; 2018.

[43] Kornev N, Hassel E. Method of random spots for generation of synthetic inhomogeneous turbulent fields with prescribed autocorrelation functions. Commun Numer Methods Eng 2007;23(1):35–43. http://dx.doi.org/10.1002/cnm.880.

[44] Pope SB. Ten questions concerning the large-eddy simulation of turbulent flows. New J Phys 2004;6. http://dx.doi.org/10.1088/1367-2630/6/1/035.

[45] Poinsot TJ, Lelef SK. Boundary conditions for direct simulations of compressible viscous flows. J Comput Phys 1992;101(1):104–29. http://dx.doi.org/10.1016/0021-9991(92)90046-2.

[46] OpenFOAM. waveTransmissiveFvPatchField Class Reference. 2021, URL (Accessed 25 February 2025).

[47] Spalding DB. A single formula for the law of the wall. J Appl Mech 1961;28(3):455–8. http://dx.doi.org/10.1115/1.3641728.

[48] Demayo T, Leong M, Samuelsen G, Holdeman J. Assessing jet-induced spatial mixing in a rich, reacting crossflow. J Propuls Power 2003;19(1):14–21. http://dx.doi.org/10.2514/2.6098.

[49] Fric T, Roshko A. Vortical structure in the wake of a transverse jet. J Fluid Mech 1994;279:1–47. http://dx.doi.org/10.1017/S0022112094003800.

[50] Fang Z, Zhang C, Liu Y, Gao T, Liu C, Xue X, Gao W, Xu G, Zhu J. Thermal mixing and structure of the jet in swirling crossflow. Phys Fluids 2024;36(9). http://dx.doi.org/10.1063/5.0222782.

[51] Dimotakis PE. Turbulent mixing. Annu Rev Fluid Mech 2005;37(1):329–56. http://dx.doi.org/10.1146/annurev.fluid.36.050802.122015.

[52] Bevilaqua PM, Lykoudis PS. Turbulence memory in self-preserving wakes. J Fluid Mech 1978;89(3):589–606. http://dx.doi.org/10.1017/S002211207800275X.